Thesis

Methodology to identify and quantify flight path dependent bird strike scenarios over aircraft

Jonas Bertholdt, 4557794

Delft University of Technology

Thesis

Methodology to identify and quantify flight path dependent bird strike scenarios over aircraft

by

Jonas Bertholdt, 4557794

Supervisor: Saullo G.P. Castro (TU Delft) & Wydo van de Waerdt (GKN Fokker)
Place: Kluyverweg 1, 2629 HS, Delft
Date: May 2024

Cover Image: Modified Version of figures 3.9, 4.14 and 4.15, background taken from adobe `https://stock.adobe.com/de/images`

Delft University of Technology
Faculty of Aerospace Engineering
Department of Aerospace Structures and Materials

Graduation Committe

Chair holder:

Dr.Ir. J.A. Pascoe
Ae. Structures & Materials

Committee members:

Dr.Ir. C.D. Rans
Ae. Structures & Materials

Dr.Ir. S.G.P. Castro
Ae. Structures & Materials

Ing. W.v.d. Waert
GKN Fokker

Dated: 31 May 2024

Preface

I want to dedicate the preface of my Thesis to the people who supported and guided me throughout the lengthy process of writing it.

First and foremost, I am thankful for my supervisors Wydo and Saullo. Your guidance and patience have been essential for the success of my Thesis. Without your expertise and mentorship, my research would not have been possible.

To Maria, your love and encouragement have been a great source of strength. Without your willingness to proofread my work and to offer feedback I could not have written the Thesis as it is now.

I am also grateful to my friends. Marco and Rolijne, your presence in the study room was a great motivator to come to university every day. Ahan, I am very grateful for your open ear for every discussion. Mathieu, your constant calls pulling me to the library made the last weeks of my Thesis extra productive. I also want to thank my countless other friends who helped me to stay positive throughout this journey.

Last but certainly not least, I want to express my gratitude to my family. Myrjam, thank you for believing in me and for the help with the cover image. Mama, Papa, your love and support have formed me, leading me down this path. Without your affirmation, I would not have come this far.

Jonas Bertholdt, 4557794
Delft, June 2024

Abstract

The demand for more efficient aircraft and new modes of transportation lead to a departure from the traditional tail and wing configuration. In order to operate an aircraft, it needs to be certified. Most Aircraft with a capacity to carry more than 10 passengers have to fulfil a variety of bird strike related certification standards. These standards define an impact velocity to design for, critical locations and tested areas however are chosen based on experience of previous aircraft. This is not possible if the design is radically different, as it is in the case of the Flying-V. The present thesis proposes a methodology to identify and rank all possible bird strike scenarios, based on geometry and flight path. The quantification of impact scenarios may offer a cost-effective way to assess and visualize vulnerabilities, ultimately reducing certification cost and time. Thereby allowing new concepts to be certified. The methodology synthesized in this report relies on decoupled analytical bird strike load models from the late 70s to quantify bird strike intensity. An algorithm has been developed to determine impact scenarios over the area of arbitrary computer aided design (CAD) geometries. Ray tracing allows for the exclusion of areas that can not be hit. The results are not sufficient to determine critical impact locations, as the damage is significantly influenced by the structural response. However, it is possible to quickly generate probable impact scenarios over large areas based on the flight path. Despite the discrepancy between predicted damage and impact intensity, intensity maps can indicate areas of interest for investigation.

Keywords: FOD, Bird Strike, Critical Impact Location, Certification, Analytical Bird Impact Model, Verification

Contents

Nomenclature

Abbreviations

Abbreviation	Definition
AC	Aircraft
ALE	Arbitrary Lagrangian-Eulerian
ALLIE	Internal Energy
ALLPD	Plastic Strain Energy
ALLIE	Elastic Strain Energy
AMC	Acceptable Means of Compliance
AOG	Aviation Ornithology Group
ARAC	Aviation Rulemaking Advisory Committee
BEA	Bureau d'Enquêtes et d'Analyses pour la sécurité de l'aviation civile
BWB	Blended Wing Body
CAAC	Civil Aviation Administration of China
CAD	Computer Aided Design
CCAR	China's Civil Aviation Regulation
CFR	Code of Federal Regulations
CS	Certification Specification
EASA	European Union Aviation Safety Agency
EOS	Equation of State
FAA	Federal Aviation Administration
FEM	Finite Element Method
FOD	Foreign Object Damage/Debris
IBIS	ICAO Bird Strike Information System
IBSC	International Bird Strike Committee
ICAO	International Civil Aviation Organisation
MTOW	Maximum Takeoff Weight
OEM	Original Equipment Manufacturer
SPH	Smoothed Particles Hydrodynamics
STL	Stereolithography, Standard Tessellation Language
TAW	Tube and Wing
USDA	United States Department of Agriculture
VMO	Maximum Operating Limit Speed
VNE	Never Exceed Speed
VH	Maximum speed in level flight with maximum continuous power

Symbols

Symbol	Definition	Unit
A	Impactor impact area	[m^2]
$A_{proj.}$	Projected Area	[m^2]
A_n	Area of Element n	[m^2]
a	Impactor Radius	[m]
B	Murnaghan EOS Material constant	[Pa]
c_p	Pressure coefficient	[-]
c_r	Release Wave Velocity	[m/s]
c_0	Sound Speed of Material	[m/s]
c_{1-6}	Polynomial EOS Material Constants	[-]
e	Eulers number	[-]
E_i	Internal Energy	[J]
F_a	Steady state force	[N]
k	Linear Hugonoit Material Const.	[-]
K	Bulk Module Lin. EOS	[MPa]
L	Impactor Length	[m]
$(L/C)_C$	Critical Aspect Ratio	[-]
n_i	Unit Normal Vector of Element i	[-]
P	Pressure	[Pa]
P_a	Steady state average pressure	[Pa]
P_H	Hugoniot Pressure	[Pa]
P_{impact}	Bird strike Probability	[-]
P_S	Steady state stag. point Pressure	[Pa]
q''	Source strength	[m/s]
r	Distance to impact centre	[m]
r_{1-4}	Distances from sources on element corners to point of interest	[m]
T	FLight Duration	[s]
t_B	Peak Pressure Impact duration	[s]
t_c	Steady State start time	[s]
t_D	Impact duration	[s]
u	Velocity field in x direction	[m/s]
u_p	Particle velocity	[m/s]
u_s	Shock Propagation Velocity	[m/s]
u_0	Impactor velocity	[m/s]
U_∞	Free stream velocity	[m/s]
V	Velocity Vector of Particle i	[m/s]
$V_{av.}$	Average Velocity of aircraft	[m/s]
v	Velocity field in y direction	[m/s]
W	Kernel Smoothing Function	[-]
w	Velocity field in z direction	[m/s]
α	Oblique Impact Angle	[deg]
α_n	Oblique Impact Angle of Element n	[deg]
β	Angle between Velocity and Normal Vector	[deg]
γ	Murnaghan EOS Material constant	[-]
$\zeta_{1,2}$	Corner coordinates of element om Z axis	[m]
$\eta_{1,2}$	Corner coordinates of element om Y axis	[m]
θ	Impact angle Barber	[-]
μ	Normalised change of Density	[-]
ρ	Density	[kg/m^3]
ρ_0	Initial Density of Impactor Material	[kg/m^3]
ϕ_{cr}	Critical Yaw angle	[deg]

Symbol	Definition	Unit
ξ_1	Constant used in Banks Pressure Distribution	[-]
ξ_2	Constant used in Leach Pressure Distribution	[-]

List of Figures

List of Tables

1 Introduction

The certification specifications of the European Union Aviation Safety Agency (EASA) state, that an aircraft has to continue the safe flight and landing after it endured bird impact at a predefined velocity and bird mass [29]. Velocities and masses differ depending on the aircraft class. It is the manufacturer's responsibility to prove to EASA's satisfaction that the design meets acceptable means of compliance (AMC). Commonly, this process includes proprietary models that have to be validated by costly experiments. Modelling different areas is a time-consuming endeavour and may need to be supplemented by destructive testing of full-size models of the area of interest. Years of testing on similar shapes allowed the industry to fall back on precedence cases to minimise the critical regions that need to be investigated for certification. The rise in annual passenger numbers and the ever-more present climate change debates lead to a heightened urge to develop more efficient aircraft. Conventional tail and wing configuration (TAW), however, have been optimised for decades and according to Martinez-Val's 2017 paper [48] are reaching an asymptote in their efficiency. Regardless of the validity of that statement, TAW aircraft have been designed since the dawn of aviation, where small improvements are still possible but very costly. There exist other configurations that promise to be more fuel efficient. However, they have not yet been further developed in the civil sector, due to other constraints like manufacturing. Such a design is the flying wing or blended wing body (BWB) aircraft. Other than facing the challenge of designing a new concept, the majority of previous experience in certificating such aircraft is irrelevant. New concepts need to be developed to meet different standards, such as emergency evacuation times, but also bird strike related ones. A changed shape leads to a change in areas that are exposed to bird strike, making the certification very costly.

The methodology presented in this report hopes to offer a reliable way to indicate the most critical bird strike scenarios depending on the impact location. Such indications have the potential to prove to the certification authorities that only certain areas need to be investigated, drastically cutting down certification costs and time. Additionally, it may be used during the preliminary design phase to visualise how the positioning of different components impacts the total area of bird strike vulnerability. To achieve this goal, two distinct things need to be predicted. Firstly, the intensity of bird impact and secondly, the bird strike scenarios depending on location and flight path.

Chapter 2 introduces the reader to the bird strike topic and further elaborates on the importance of this research. The methodology is laid out in chapter 3, breaking down all assumptions and models utilised. Chapter 4 demonstrates and discusses different aspects of the methodology. It follows chapter 5 concluding the findings of chapter 4. Finally, the recommendations for further improvement of the methodology are given in chapter 6.

2
Motivation

This chapter contains the foundation and motivation of the thesis. It provides an overview of the bird strike topic, current certification standards and the impact of novel aircraft design on both.

Section 2.1 provides a brief introduction to the bird strike topic. It follows section 2.2, which introduces the certification standards that any manufacturer needs to meet to acquire permission to sell and fly their aircraft. Finally, section 2.3 elaborates on the importance of the following study and formulates a research objective.

2.1. Introduction to Bird Strike

This section aims to provide a concise overview of all aspects of bird strike important for the research objective.

Subsection 2.1.1 offers an overview of bird strike statistics. The following subsection 2.1.2 showcases possible bird strike consequences and elaborates on damage distributions. Finally, subsection 2.1.3 contains a description on how new aircraft concepts may be affected by bird strike.

2.1.1. Bird Strike statistics

Bird strike or wildlife strike is categorised as foreign object damage/debris, FOD in short. Even though some define bird strike as a collision between an aircraft and an airborne creature, the term is often expanded to include all wildlife. Most times, bird strike is fatal for the animal. However, the damage to the aircraft can range from stains to catastrophic failure [37, 58].

Although bird strike is a rare occurrence, as seen in Table 2.1, its cost for the civil aviation industry is significant. J.R. Allan's 2000 paper [9] estimates the cost of bird strike to be US$ 1.2 billion or US$ 64.5 per flight in the USA alone. The average cost per bird strike incident is US$ 49,705.

Table 2.1: Average bird strike rates (number of strikes per 10,000 aircraft movements) [53]

Country	Bird Strike Rate	Period Considered	Source
Australia	7.76	2008-2017	[11]
Canada	3.51	2008-2018	[53]
France	3.95	2004-2013	[25]
Germany	4.42	2010-2018	[24]
UK	7.76(all) 4.62(confirmed)	2012-2016	[62]
USA	2.83	2009-2018	[27]

Bird strikes have been a concern since the very beginning of powered flight. Orville Wright collided with a bird in 1905, just 2 years after his historical first flight, marking the earliest documented bird strike incident. Just 7 years later, in 1912, the first fatal incident was recorded, when Calbraith Rodgers died due to injuries obtained in a crash caused by bird strike.

These accidents, however, remained freak accidents. As seen in Figure 2.1 the number of catastrophic bird strike incidences in the civil sector remained under 10 per decade up to 1970. In the time period between 1912 and 1959, only two fatalities due to bird strike are known. Figure 2.2 shows the number of fatalities per decade due to bird strike in a period from 1901 to 2010. The spike in the 50s can be attributed to a single incident, that marks the deadliest accident in bird strike history. On October 4th, 1960 Eastern Airlines Flight 375 crashed during takeoff at the Logan International Airport in Boston, Massachusetts. Approximately six seconds after lift off, the aircraft encountered a flock of starlings, resulting in the loss of several engines. The ensuing crash cost 62 people their lives. This incident heightened the awareness about the risks of bird strike and the need for risk mitigation strategies.[26, 37, 58]

Both Figure 2.1 and 2.2 from Dolbeer's 2013 report [26] show an increasing impact of bird strike incidences. There is not just an increase in catastrophic bird strikes, but also an increase in the number of bird strikes, as noted in the 2000 Report of the United States Department of Agriculture (USDA) [21]. Just in the USA, a 181% increase of reported bird strikes between 1999 and 1998 has been recorded. Also, newer reports like Dolbeer's 2021 study [27] as well as world-wide observations like El-Sayed's [58] or Hedayati et al.'s books [37] note an increase in bird strike incidences. Three main factors are often accredited for this development.

Firstly, the increased speed of aircraft, as well as the reduced noise of engines. Both speed and noise impact the bird's ability to detect and avoid an aircraft. According to Hedayati et al. [37], a fact that supports this hypothesis is that more bird incidences occur during landing than take off. He theorizes that this is the case because the engines emit more noise during take-off, underlining the importance of noise. Doolbeer underlines the importance of speed in his 2013 report. Higher speeds result in more destructive collisions, causing a rise in damages in the statistics.

Secondly, the quickly growing civil air traffic sector. Over the last 70 years, flying has become cheaper and the amount of air traffic has risen consistently, ignoring the recent pandemic. From 1980 to 2019, the number of annual passengers has increased significantly from 0.8 billion to 4.6 billion.[1].

Lastly, changes in wildlife populations. Decade long efforts in wildlife preservation show effect, increasing the population of a variety of species all over the world. A. El-Sayed's 2019 book on bird strike statistics and management [58] acknowledges an increase of large bird species in North America and its effect on bird strike statistics. For instance, the Canadian geese population ballooned from 500,000 in 1980 to 3.8 million in 2013. Other analyses of the bird strike development, like Dolbeer[27] and Hedayati [37], make similar observations.

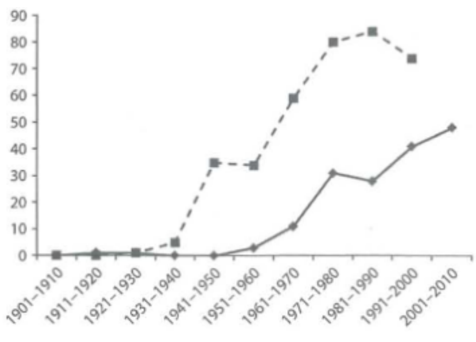

Figure 2.1: Number of Aircraft destroyed due to bird strike per decade, the dotted line represents military and the solid line civil Aircraft. Taken from [26]

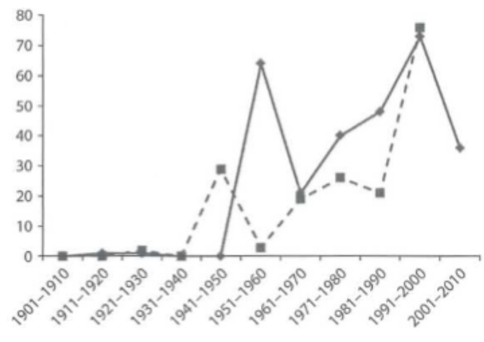

Figure 2.2: Number of Human fatalities due to bird strike per decade, the dotted line represents military and the solid line civil Aircraft. Taken from [26]

Figure 2.3 depicts the correlation between altitude, number of impacts and percentage of damaging bird strike incidences. It is interesting to note that the higher the aircraft's altitude, the lower the likelihood of an incident. Nevertheless, the percentage of damaging bird strikes behaves oppositely. The increase in damaging impacts can be explained by the correlation of speed and altitude. In general, aircraft operate at higher speeds the higher they are flying and higher speed impacts have more energy, making them

[1] `https://www.iea.org/data-and-statistics/charts/world-air-passenger-traffic-evolution-1980-2020`, 01.04.2024

more dangerous. It is also interesting to note that almost all incidences occur under 400 ft. Meaning that most bird strikes happen during take-off, climbing, approach and landing. Even though that is the case, a risk of bird strike is present during all stages of flight, as the highest recorded bird strike occurred at 37,000ft [2], which is above the cruise altitude of most commercial jets.

The International Civil Aviation Organisation (ICAO) published a wildlife strike analysis [1] based on the Bird Strike Information System (IBIS), which collects data on bird strikes in over 105 states and territories. According to the report, 90% of all bird strikes occur during landing (26%), approach (33%) and take-off (31%). It is also concluded that the majority of bird strikes happen during the day. The United States Department of Agriculture (USDA) report of 2021 [27] concludes that 62% of bird strike incidences occur during the day, 30% during the night and 4% each during dawn and dusk.

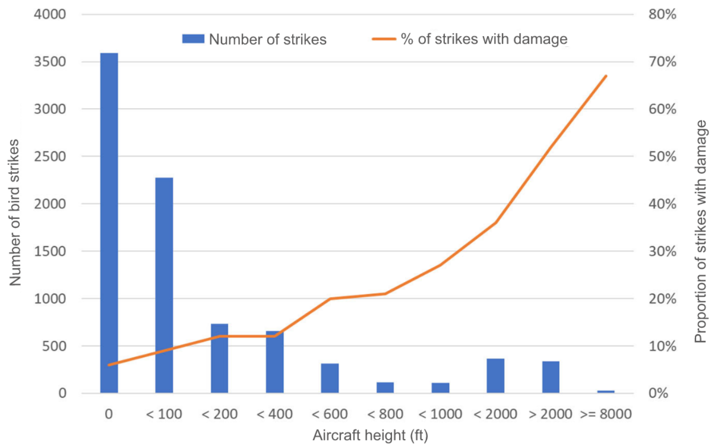

Figure 2.3: Number of bird strikes and proportion of damaging strikes over altitude taken from [39]

2.1.2. Bird Strike Damage

L.S. Nizmpatnam lists the unique characteristics of bird strike in his 2007 thesis [54]. He highlights the violent and short impact, as well as the dynamic coupling between the impactor and target. Both undergo high inelastic strain. The damage depends on both the impact velocity and orientation, as well as the location that is hit. Collisions at low velocities may not only result in a smudge on the windshield but could also lead to engine failure or damage to important sensors like angle of attack indicators or pitot tubes. The same can be said about high-speed impacts. Birds may bounce off the fairing, leaving a small dent, or may damage critical parts like avionics or the radar dome. Impacts may reach pressures of 300MPa and only last 4-10 milliseconds. Figure 2.4 to 2.6 contain images of three bird strike incidences occurring on different size aircraft.

The first image seen in Figure 2.4 depicts damage to the radar dome of a Boeing 737-900. A large bird hit the aircraft during the approach phase, penetrating the radar dome and damaging the pitot tubes. The damaged pitot tubes led to a loss of airspeed information, forcing the pilots to rely on ground speed readings provided by ground control to land safely.[3]

Figure 2.5 shows a damaged leading edge of a small propeller aircraft.

The damage seen in Figure 2.6 led to the death of one pilot and an injury to the other. One engine was damaged after ingesting windshield debris, forcing the pilot to shut it down. Additionally, the hydraulic system was damaged, leading to the loss of breaks and flaps. The pilot managed to land the aircraft safely [61].

More comprehensive collections of bird strike incidences can be found in reports of the U.S. Department of Agriculture like Dolbeer et al.'s 2021 report [27], Thorpe's 2003 report [61] or chapter 2 of El-Sayed's 2019 book on bird strike [58].

[2] `https://www.historynet.com/when-birds-strike/`, 02.04.2024
[3] `http://avherald.com/h?article=45395ad3`, 25.03.2024

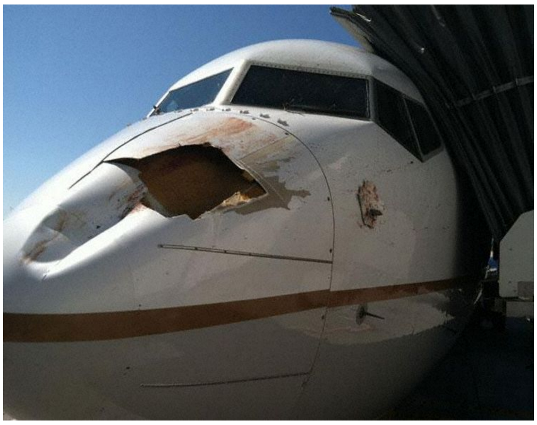

Figure 2.4: B737 Nose Cone Damage [58]

Figure 2.5: Small Aircraft Wing Damage [58, 17]

Figure 2.6: Lear 35A Windshield Damage [61]

Table 2.2 offers an overview of the bird strike distribution over different parts of an aircraft. The data was collected out of different sources, and the most common divisions were chosen for the table. The spread between the 5 sources is quite big. To decrease the spread one may take into account the origin of the data. The first three entries from Airbus [6], Boeing [18], and the Aviation Ornithology Group (AOG)[12] are all exclusively taking airliner data into account. ICAO [1] and USDA [27] however, include all types of planes.

For the airliner data, it seems that the engines are hit most often, followed by the aircraft front (Radome/Nose and Windshield) and the wings.

Furthermore, 4-12% of impacts hit the fuselage. At first glance, this may appear counter-intuitive, as the fuselage is mostly parallel to the flight path. However, the high angle of attack during take-off and landing exposes the belly, explaining the high number of collisions.

The methodology proposed in this report can quantify the exposed area based on the flight path. This allows for the comparison of designs and flight states in terms of vulnerable areas.

Table 2.2: Percentage of hits in ac parts taken from Airbus[6],Boeing[18], AOG[12], ICAO[1] and USDA [27]

	Sources				
Affected area	**Airbus %**	**Boeing%**	**AOG %**	**ICAO %**	**USDA %**
Radome/Nose	41	8	4.9	27	25.7
Windshield		13	6.7	15	15.4
Engines	41	44	48.9	15	13.2
Fuselage	7	4	9	12	11.2
Landing gear	3	-	6.7	12	4,3
Wing	7	31	21.1	16	13.9
Tail	1	-	2.7	1	1.2
Other	-	-	-	2	15

Both ICAO's [1] and USDA's [27] wildlife strike reports provide additional data about the number of strikes resulting in damage. Figure 2.7 visualizes this data as a bar diagram and also contains the percentages of damaging impacts.

The most vulnerable area are the lights, which despite their low amount of hits are damaged by 35-60% of the time when they are impacted. A similarly fragile part appears to be the empennage, where roughly 30% of impacts lead to damage. Birds hitting engines result in damage in 15% to 23% of cases. Between 12% and 18% of hits to the wing lead to damage [1, 27].

However, damage may not always lead to catastrophic failure. Thorpe's 1912-2002 Bird strike study, reported to the International Bird Strike Committee (IBSC), [61] states that 77% of incidences leading to fatalities and/or the loss of an aircraft over 5700 kg are the result of engine damage. The second most common cause is bird strike to windshields with 10% of the cases. However, this number skyrockets to 52 % when aircraft under 5700kg are taken into account. This is the result of a different set of certification standards for smaller aircraft [61]. As elaborated in subsection 2.2.3, small aircraft under 10 passengers have no bird strike-related certification standards (CS). Small aircraft with more passengers have to prove that a 2 lb bird can not penetrate the structure in front of the pilots at maximum approach flap speed. Large aircraft have increased CS as the bird mass is increased to 4 lb and the velocity a percentage of the cruise speed [33, 30, 29, 32, 31].

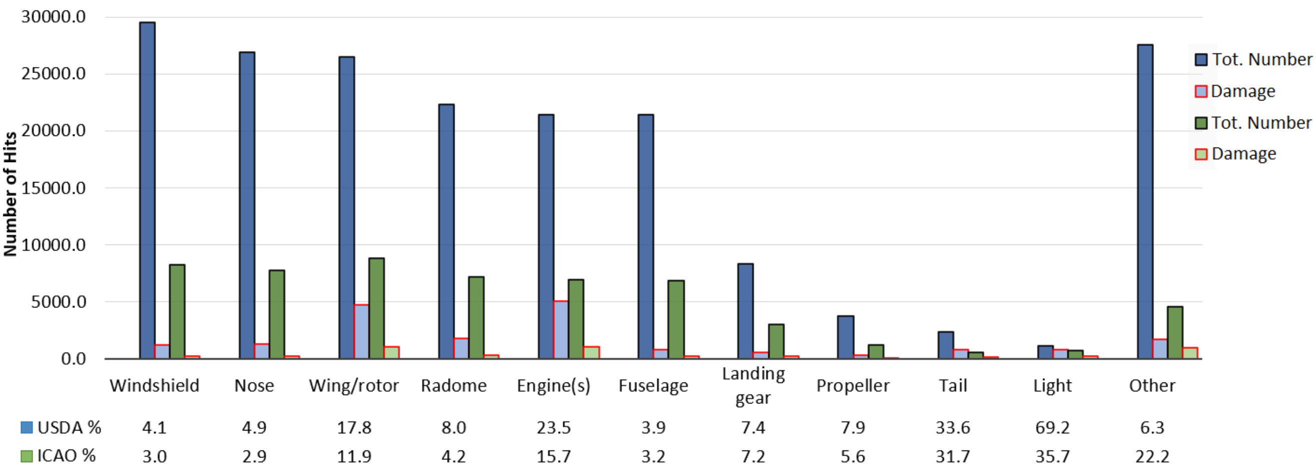

Figure 2.7: Number of hit parts and damaged parts taken from ICAO Wildlife strike analysis [1] and USDA [27]

2.1.3. Bird strike and New Aircraft Configurations

The statistics summarized by subsection 2.1.1 and 2.1.2 are important to understanding bird strike. In any case, they are not universally applicable. The widespread of data in Table 2.2 already demonstrated that different aircraft types present different problems. Changes in operational ranges, flight path profile and geometry of the aircraft influence the vulnerability to bird strikes. Therefore, it is imperative to understand the effects new aircraft configurations may have on bird strike risk management.

Figure 2.8 and 2.9 compare the Flying-V, a blended wing body (BWB) concept, to its tail and wing

(TAW) configuration counterpart, the A350-900. When inspecting Figure 2.8, the overall vulnerable area appears similar in size. However, due to the configuration change, the fuselage and wings are merged for the Flying-V. This means that not just the cockpit, but the whole fuselage is exposed to bird strike. Additionally, the airfoil at the fuselage area is a lot thicker than the airfoil of a conventional wing, increasing the forward-facing area drastically. However, some advantages may arise from a changed design. As seen in Figure 2.9, the engines of the Flying-V are shielded by its body. This may reduce the amount of bird ingestions and could lead to a safer aeroplane.

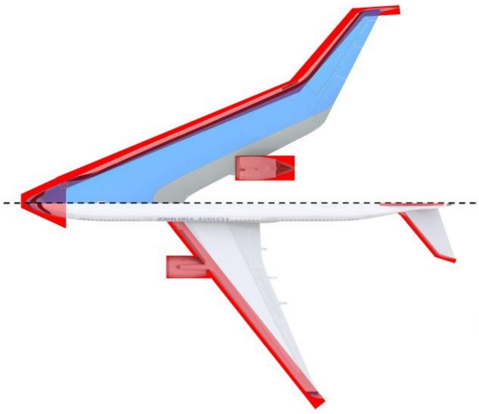

Figure 2.8: Bird strike critical zones Flying-V and A350-900 cruise phase [4, 64]

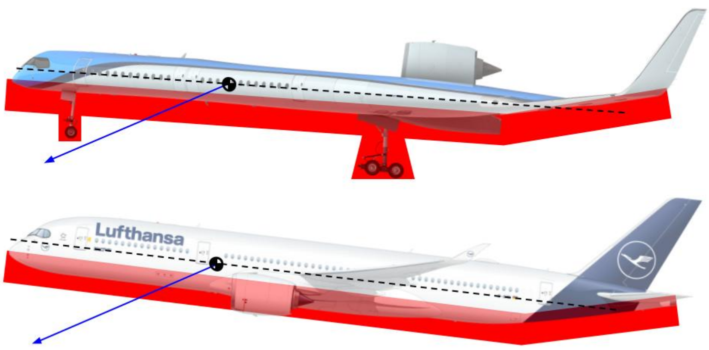

Figure 2.9: Bird strike critical zones Flying-V and A350-900 landing phase, original Images taken from [7, 64]

There have been some studies regarding the impact of bird strikes on flying wing designs, although they are not very common. One such study was conducted by Chen et al. in 2022 [20].

In this study, the researchers investigated the damage caused by bird strikes on a Flying-V fuselage approximation and identified the critical location of impact. They created a detailed finite element model (FEM) of a typical fuselage section and modelled sixteen impact locations using the SPH method (Smoothed Particle Hydrodynamics). The study found that the location above the centre line of the window leads to the highest plastic strain energy and is therefore the most critical location for potential damage. The researchers also changed the thicknesses of the skin, frame, and pane clamp to evaluate their impact on the structure's resilience. They found that the pane clamp has the most significant influence on the structure's performance.

The study concluded that the structure is capable of withstanding bird strikes of up to 70 m/s without any damage and can withstand certification-specified impacts without penetration.

The results are not directly applicable to the Flying-V design, as its fuselage design differs significantly from Chen et al.'s fuselage cross-section, which was greatly inspired by conventional aircraft. The frames of the current Flying-V design are four times higher, and no window design has been integrated as of now [20, 23, 28, 35, 41, 63].

Despite these differences, the study demonstrates that with the change of configuration, the bird strike requirements become critical for the fuselage design. Especially the common window architecture has to be rethought, as it is not designed for impact. The differences in architecture become apparent when comparing windows that are designed to withstand bird strike to those that are not.

Figure 2.10 illustrates the structure of a cockpit as presented in Marulo et al.'s 2014 paper on bird strikes [49]. Chen et al.'s study used the window geometry shown in Figure 2.11. The windows in Figure 2.10 are integrated directly into the frames, allowing for better force transfer into the surrounding structure. In contrast, the windows in Figure 2.11 are fastened only to the skin and are at the maximum distance from the frame and stringers. Chen's windows are made of a single pane of polycarbonate, whereas windshields are typically laminates made from several materials to optimize bird strike resistance. Whether it is possible to integrate windows along the fuselage without significantly increasing weight remains uncertain [20, 49, 50].

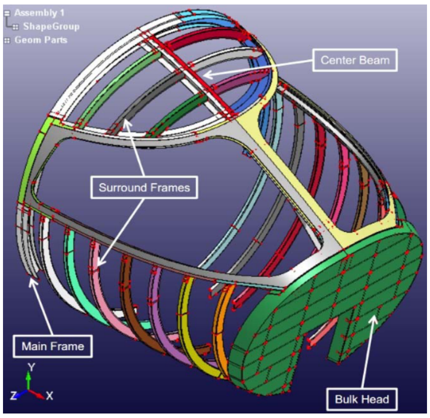

Figure 2.10: Cockpit Structure with integrated window frames [49]

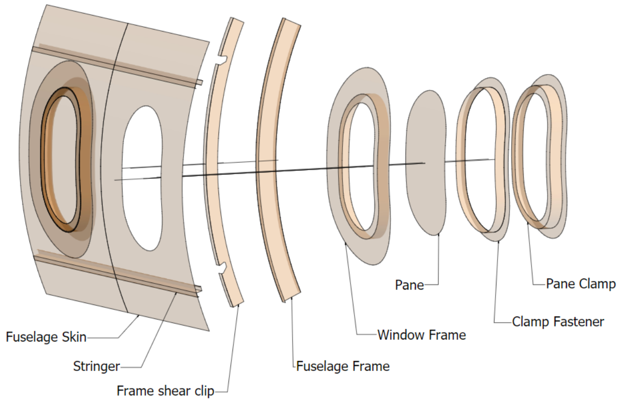

Figure 2.11: Explosion drawing of Chens LE geometry of FLying-V taken from [20]

Air travel is not just evolving to be more efficient. There are also new concepts that may become accessible to the public, like vertical take-off and landing (VTOL) vehicles. These aircraft concepts have already been in use within the military sector for decades, due to their ability to land and take off from small spaces. Several companies are developing VTOL vehicles, mainly as air taxis in an urban air mobility scenario.

Figure 2.12 depicts such a concept taken from Palaia et al.'s 2021 design concept study [55]. In this study, a design methodology for a tilt-wing VTOL vehicle is introduced. Whilst this design only has a cruise speed of 45 m/s, other VTOL vehicles, such as the Prosperity I, aim for speeds of 70 m/s[4].

Even though these speeds may seem low when compared to larger aircraft, they are already in a range that may result in catastrophic failure. The 2021 incident report of the Bureau d'Enquêtes et d'Analyses pour la sécurité de l'aviation civile (BEA) [39] describes a bird strike incident that cost 3 lives. A DR400-140B aircraft collided with a cormorant at an estimated speed of 50 m/s, leading to the loss of a lifting surface.

VTOL aircraft are capable of morphing, allowing them to hover like a helicopter but also to fly like a plane. However, this ability to switch between different flight modes poses a challenge to current certification standards. The areas highlighted in red in Figure 2.12 depict how the change in flight mode can affect the areas that are susceptible to bird strike. Defining what areas are hit, and how they will be hit, is paramount to certifying these aircraft concepts as well as in aiding new certification standards [55].

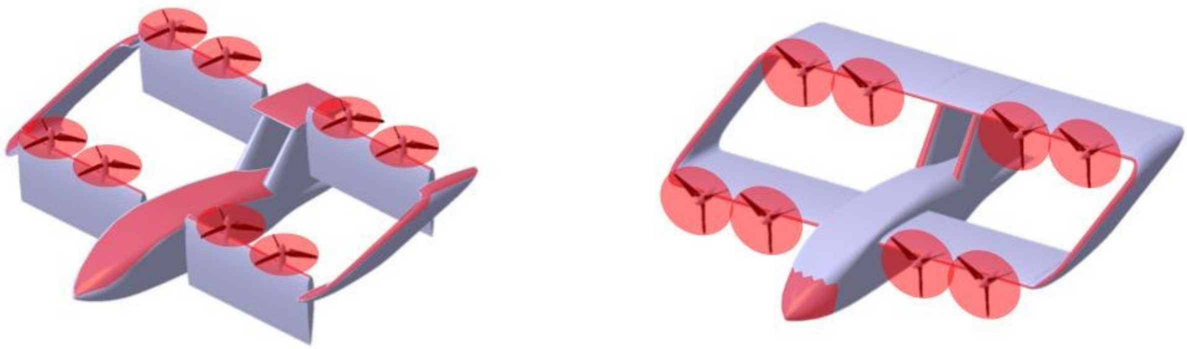

Figure 2.12: Bird strike critical zones of VTOL concept take from [55]

2.2. Certification

The following section introduces bird strike certification requirements and how they may be affected by new aircraft concepts.

[4] `https://evtol.news/autoflight-v1500m`, 04.04.2024

Section 2.2.1 lists all relevant FAA regulations. The following subsection 2.2.2 presents the European regulations. Finally, subsection 2.2.3 summarizes the regulations and offers some commentary.

There exist almost as many regulatory bodies for aviation as countries. Each has its own standards, certification procedures and amendments. Despite the ICAO's efforts to standardize safety standards, no worldwide regulation standards exist as of now. To summarize the current state of bird strike regulations 2 major regulatory buddies are compared. Firstly, Title 14 of the Code of Federal Regulation (CFR) [34], which contains all Federal Aviation Administration (FAA) regulations for the United States. Secondly, the European Union Aviation Safety Agencies (EASA) Certification Specifications for normal aeroplanes (CS-23 [30]), large aeroplanes (CS-25 [29]) and small as well as large rotorcraft (CS-27 [32], CS-29 [31]). China's Civil Aviation Regulation (CCAR) Airworthiness Standard [19], reinforced by the Civil Aviation Administration of China (CAAC), is a word for word copy of title 14. Therefore it is not included in the regulation analysis. The following paragraphs contain all certification standards regarding bird strike on fuselage, windows and windshields, as these are the main focus of the thesis.

2.2.1. FAA Regulations

The certification specifications taken from part 23 of title 14 of the CFR [34] are airworthiness standards of normal category airplanes. A normal category airplane is defined by §23.2005: All airplanes with a passenger seating of 19 or less and a maximum takeoff weight of 19,000 pounds (8.6t). The only regulation regarding birds is found in §23.2320 and limits itself to level 4 airplanes. A level 4 airplane is a normal category airplane with 10 to 19 passengers and is, therefore, the biggest category described in §23.2005[34].

- **§23.2320 Occupant physical environment:**

  (b) "*For level 4 airplanes, each wind shield and its supporting structure directly in front of the pilot must withstand, without penetration, the impact equivalent to a two-pound bird when the velocity of the airplane is equal to the airplane's maximum approach flap speed.*""[34]

All specifications defined in part 25 of title 14 of the CFR [34] are airworthiness standards for transport category aircraft. Transport category aircraft is not defined by their maximum takeoff weight (MTOW) and may include helicopters. Nevertheless, there are examples of aircraft that are typically categorised as such [5]:

- Jets with 10 or more passenger seats and or an MTOW of 12,500 pounds (5.7t) or more.
- Propeller driven airplanes with more than 19 passengers and or an MTOW of 19,000 pounds (8.6t) or more.
- Helicopters with an MTOW higher than 7,000 lb (3.1t).

However, FAA may categorise aircraft as transport airplanes, that are not within these specifications, depending on the engine type used and date of certification.

- **§25.571 Damage-tolerance (discrete source) evaluation:**

  (e) "*Damage-tolerance (discrete source) evaluation. The airplane must be capable of successfully completing a flight during which likely structural damage occurs as a result of*—"[34]

    1 "*Impact with a 4-pound bird when the velocity of the airplane relative to the bird along the airplane's flight path is equal to Vc at sea level or 0.85Vc at 8,000 feet, whichever is more critical*" [34].

  "*The damaged structure must be able to withstand the static loads (considered as ultimate loads) which are reasonably expected to occur on the flight. Dynamic effects on these static loads need not be considered. Corrective action to be taken by the pilot following the incident, such as limiting maneuvers, avoiding turbulence, and reducing speed, must be considered. If significant changes in structural stiffness or geometry, or both, follow from a structural failure or partial failure, the effect on damage tolerance must be further investigated*" [34].

[5] https://skybrary.aero/articles/transport-category-aircraft, 04.04.2024

- **§25.631 Bird strike damage:**
  ”*The empennage structure must be designed to assure capability of continued safe flight and landing of the airplane after impact with an 8-pound bird when the velocity of the airplane (relative to the bird along the airplane’s flight path) is equal to VC at sea level, selected under § 25.335(a). Compliance with this section by provision of redundant structure and protected location of control system elements or protective devices such as splitter plates or energy absorbing material is acceptable. Where compliance is shown by analysis, tests, or both, use of data on airplanes having similar structural design is acceptable*” [34].

- **§25.773 Pilot compartment view:**

  (b) ”*Precipitation conditions. For precipitation conditions, the following apply:*”

  (4) ”*The openable window specified in paragraph (b)(3) of this section need not be provided if it is shown that an area of the transparent surface will remain clear sufficient for at least one pilot to land the airplane safely in the event of*”

  (ii) ”*an encounter with severe hail, birds, or insects.*”

- **§25.775 Windshields and windows:**

  (b) ”*Windshield panes directly in front of the pilots in the normal conduct of their duties, and the supporting structures for these panes, must withstand, without penetration, the impact of a four-pound bird when the velocity of the airplane (relative to the bird along the airplane’s flight path) is equal to the value of VC, at sea level, selected under § 25.335(a)*” [34].

  (c) ”*Unless it can be shown by analysis or tests that the probability of occurrence of a critical windshield fragmentation condition is of a low order, the airplane must have the means to minimize the danger to the pilots from flying windshield fragments due to bird impact. This must be shown for each transparent pane in the cockpit that -*” [34]

  1. ”*Appears in the front view of the airplane;*” [34]
  2. ”*Is inclined 15 degrees or more to the longitudinal axis of the airplane; and*” [34]
  3. ”*Has any part of the pane located where its fragmentation will constitute a hazard to the pilots*” [34]

- **§25.1323 Airspeed indicating system:**

  (j) ”*Where duplicate airspeed indicators are required, their respective pitot tubes must be far enough apart to avoid damage to both tubes in a collision with a bird*” [34].

All specifications defined in part 29 of title 14 of the CFR [34] are airworthiness standards for transport category rotorcraft (Category A and B). A rotorcraft is defined as heavier-than-air aircraft that depends on the lift generated by one or more rotors to fly[6]. The differentiation between category A and B is defined at §1.1 *Category* (2) and in §29.1 [34]. The most important difference between the two categories is, that category A rotorcraft have multiple engines and operate under a critical engine failure concept. Meaning, that it possesses adequate surface area designed to guarantee safe flight in the event of engine failure. A category B rotorcraft may be single or multi-engine and does not posses a guaranteed stay-up ability [34].

- **§29.631 Bird strike:**
  ”*The rotorcraft must be designed to ensure capability of continued safe flight and landing (for Category A) or safe landing (for Category B) after impact with a 2.2-lb (1.0 kg) bird when the velocity of the rotorcraft (relative to the bird along the flight path of the rotorcraft) is equal to VNE or VH (whichever is the lesser) at altitudes up to 8,000 feet. Compliance must be shown by tests or by analysis based on tests carried out on sufficiently representative structures of similar design*” [34].

[6] https://www.law.cornell.edu/definitions/index.php?width=840&height=800&iframe=true&def_id=1e9a932548a5f86147053391fb958501&term_occur=999&term_src=Title:14:Chapter:I:Subchapter:A:Part:1:1.1,04.04.2024

2.2.2. EASA Regulations

Most of the EASA Regulations are directly inspired by Title 14. To avoid direct copies, each bird strike relevant CS is listed beneath with a small description listing if there is any differences to the FAA regulation. Only original paragraphs are quoted.

The specifications are taken from CS-23 for normal aeroplanes, just like part 23 of Title 14. Normal aeroplanes are separated into four levels, and the only bird strike specific CS is restricted to level 4 aeroplanes. The definition of such aircraft is the same as Title 14s level 4 airplanes and can be found in CS 23.2005 [30].

- **CS 23.2320 Occupant physical environment**

  (b) Copy of Title 14 §23.2320.[30, 34]

The certification specifications taken from CS-25 [29] are airworthiness standards for large aeroplanes. Unlike the transport aircraft category of the FAA, EASA's large aeroplanes are defined by their MTOW. All aircraft with a MTOW higher than 5,700kg (12,500lb), except for the commuter aeroplane category, are deemed large aircraft.[33]

- **CS 25.571 Damage tolerance and fatigue evaluation of structure**

  (e) Nearly identical to Title 14 §25.771 (e). The impact scenario description is taken from CS 25.631. Only bird strike is mentioned as a cause of damage [29, 34].

- **CS 25.631 Bird Strike damage**
  "*The aeroplane must be designed to assure capability of continued safe flight and landing of the aeroplane after impact with a 4 lb bird when the velocity of the aeroplane (relative to the bird along the aeroplane's flight path) is equal to VC at sealevel or 0·85 VC at 2438 m (8000 ft), whichever is the more critical. Compliance may be shown by analysis only when based on tests carried out on sufficiently representative structures of similar design*" [29].

- **AMC 25.631 Bird Strike Damage**
  "*Consideration should be given in the early stages of the design to the installation of items in essential services, such as control system components, and items which, if damaged, could cause a hazard, such as electrical equipment. As far as practicable, such items should not be installed immediately behind areas liable to be struck by birds*" [29].

- **CS 25.773 Pilot compartment view**

  (4) Copy of Title 14 §25.773 (b)(4)(ii) [29, 34].

- **CS 25.775 Windshields and windows**

  (b) Nearly identical to Title 14 §25.775 (b). The impact scenario, however, is taken from CS 25.631 [29, 34].
  (c) Copy of Title 14 §25.775 (c) [29, 34].

- **CS 25.1323 Airspeed indicating system:**

  (j) Copy of Tirl 14 §25.1323 (j).[29, 34]

The certification specifications taken from CS-27 [32] are airworthiness standards for small rotorcraft. Rotorcrafts are defined identically by the FAA and EASA. A small rotorcraft is defined by CS 27.1 (a) as a rotorcraft weighing less than 3,175 kg (7,000 lb) and having a maximum of nine passenger seats [33, 32].

- **CS 27.631 Bird strike** Nearly identical to Title 14 §29.631. Nonetheless, limited to rotorcraft with 6 or more passenger seats and no mention of category A or B [32, 34].

The certification specifications taken from CS-29 [32] are airworthiness standards for large rotorcraft. Generally, large rotorcrafts are heavier than 3,175 kg (7,000 lb). Similar to the FAA, EASA distinguishes between category A and B rotorcraft. In any case, EASA uses slightly different criteria for the division, which can be found in CS29.1. It may be interesting to note that the requirements of CS 29.631 are described in more detail in AMC1 29.631 [33, 32].

- **CS 29.631 Bird strike** Copy of Title 14 §29.631 [31, 34].

2.2.3. Summary & Discussion

Comparing the regulations, it is apparent that even though there does not exist a universally applicable certification specifications document, all regulatory bodies adhere to very similar rules. Even the numbering for certain regulation topics is equivalent. EASA, however, has clarifying paragraphs called Acceptable Means of Compliance (AMC) that add information about the CS.

The only differences, even though minute, that are present are the definitions of different aircraft categories and some details on the definition of impact scenarios.

The definition of normal-category airplanes is the same for all, but large-category airplanes have a different definition. To determine which aircraft can be classified as large-category, the FAA uses more general terms and decides on a case-by-case basis. On the other hand, EASA sets a minimum MTOW of 57,000kg. No case of mismatched categories between the FAA and EASA is known.

EASA categorizes rotorcraft into small and large, while FAA only has one category, but the bird strike regulations are the same for both.

The biggest difference in regulation is the inclusion of the 8 lb bird by the FAA. EASA only requires the certification with 4 lb birds. On the other hand, the FAA requires the empennage structure to be certified for bird strike of an 8 lb bird [33, 30, 29, 32, 31].

There have been efforts to change Title 14. In 2015, the FAA published a report to evaluate if Title 14 is still up to date [57]. Nevertheless, since the 70s no changes have been made to the bird strike related regulations of Titel 14. In 2003 the Aviation Rulemaking Advisory Committee (ARAC) proposed to wave the inclusion of the 8 lb bird in favour of the consistent use of the four-pound bird for certification similar to EASA's regulations. However, the proposal was declined by the FAA.

Besides offering an inside in Titel 14's history, the 2015 report [57] concludes with several recommendations and commentary on existing rules for transport category aircraft.

All bird strike criteria summarised in subsection 2.2.1 and 2.2.2 have single bird impact criteria, even though birds often move in flocks. The FAA justifies this by assuming that as long there exists robust CS about significant impacts in any one area, the hazard is not compounding from impacts in other areas [57].

Titel 14's §25.773 and §25.775 as well as EASA's CS 25.773 and CS 25.775 are only focused on the windshield and their supporting structure. Therefore no non penetration regulation exists for other cockpit structures, despite several recorded incidents of birds penetrating through other locations like service hatches [57].

The kinetic energy of the impacting bird is identified as the primary indicator of the severity of the impact. The report [57] contains a small study of four North-American bird incidence databases to see how often the estimated kinetic energy of the bird exceeded the limit set by the 4 lb bird of §25.571 (e). Over the span from 2008 to 2013, only 9 cases are listed. Showcasing that the majority of impacts are within the criterion.

Kinetic energy is proportional to the bird mass times impact velocity squared. Therefore, reducing the velocity is the most effective way to reduce impact severity. Many countries like the USA, Canada, Mexico and all European countries already limit the speed of aircraft that fly under 10,000 ft to 250 kts (128.611 m/s). The FAA's report [57] proposes two changes to §25.571 (e) [34].

Firstly the expansion of the cruise speed altitude from 8,000 to 10,000 ft. According to Dolber et al's study [27] 98% of all damaging bird strike incidences occur under 10,000 ft, whilst 95% of damaging incidences occur under 8,000 ft. An increase in the altitude would lead to a more robust criterion, further reducing the amounts of incidences where the kinetic energy exceeds the CS [57].

Secondly, the report proposes to change the criterion from cruise speed (V_C) to the maximum operational limit speed (V_{MO}). Some manufacturers already reduce V_C under 8,000 ft to meet the current regulations. According to the FAA, speed reductions may be encouraged by basing criteria on V_{MO}. Furthermore, speed cutbacks of the manufacturers will not just increase the safety of aircraft operation in the areas where Titel 14 is used, but all other regions as well [57, 34].

In general, the regulations can be split into three categories: regulations for normal aircraft, large aircraft and rotorcraft. Large (heavy) rotorcraft, anyhow, may be categorized as large aircraft. Large aircraft are regulated most extensively. The following lists will provide a short generalisation of the aircraft category and summarize the most important regulations.

Normal level 4 Aircraft
An airplane with 10 to 19 passenger seats and MTOW of maximal 19,00 lb (8.6 t).

1. No penetration of the structure in front of the pilots must be assured for the impact of a 2 lb bird, with a velocity of the aeroplane's maximum approach flap speed.

Large Aircraft
A large aircraft is defined by EASA as an aircraft with than MTOW higher than 5,700 kg (12,500 lb), excluding normal aircraft. Even though the FAA has a more complicated definition, no case of both institutions disagreeing is known. The 8 lb regulation is excluded from the following summary of regulations.

1. All following requirements mentioning bird strike follow the following impact scenario. Impact of a 1.8 kg (4 lb) bird at cruise speed VC at sea level, or 0,85 VC at 8,000 ft depending on the more critical case.
2. The aircraft must be able to safely complete its flight after impact.
3. Windshields and their surrounding structure must be able to withstand bird strike without penetration.
4. Windshield must be non-splintering.
5. Redundant sensors need to be placed apart, to avoid damaging both during bird strike.

Rotorcarft
Rotorcraft of category A have either 2 engines or have a means to guarantee flight after engine failure. Category B includes all other rotorcraft.

There are additional characteristics distinguishing categories A and B, although they are inconsequential to the regulation.

1. All following requirements mentioning bird strike adhere to the ensuing impact scenario: Impact of a 0.9 kg (2 lb) bird at never exceed speed (VNE) or maximum speed in level flight with maximum continuous power (VH), under 8,000 ft depending on the more critical case.
2. The rotorcraft must be able to continue safe flight (category A) or safe landing (category A and B) after impact.

When listing the regulations concisely, it becomes apparent that new aircraft configurations will force the regulating bodies to adjust.

The Flying-V and similar concepts expose the passenger cabinet to bird strike, which is not mentioned in regulations. Under current regulations, the penetration of bird mass into the cabinet would not be of concern, as long as safe flight is guaranteed. Therefore, it can be expected that additional clauses will be added to include all pressurized areas of the aircraft. Additionally, the non-splintering requirement of the windshield panes will likely be expanded to the passenger windows.

Most likely, most VTOL concepts will fall under both the normal aircraft and the rotorcraft category. Small VTOLs may even only fall in the rotorcraft category as they have less than 10 passenger seats. The main concern for these concepts is the definition of likely bird strike scenarios, as different flight modes require different scenarios.

2.3. Research Purpose/ Objective

Due to the climate crisis, the need for resource-considerate travel is vital. To achieve this, a change from the typical TAW is needed, as this concept is asymptotically reaching its maximum potential. BWB concepts, like the Flying-V, are promising to be the next step towards more efficient flight [48, 15].

Additionally, recent progress in battery technology has increased the interest in electric aviation. Such aircraft may not be able to travel vast distances, but could offer a new efficient way of traveling through metropolitan areas. One concept that is often mentioned in this context is VTOL aircraft [55, 59].

As shown in section 2.1, bird strike risk is very dependent on the design and operation of the aircraft. Up to this point, manufacturers could rely on over 100 years of bird strike records and decades of experience in certifying TAW aircraft. Usually, certifying an aircraft is a long process that relies on the dialogue between the original equipment manufacturer (OEM) and the regulatory body. Often, archival data is used to justify critical impact locations and the choice of real-life tests to prove compliance to certification specifications. However, frequency of impact, critical impact locations and scenarios are all influenced by the shape and operation of the aircraft. Therefore, a new concept may render previously sufficient analysis methods inappropriate for certification.

Consequently, it is imperative to develop new tools that can be used to predict how these changes will affect bird strikes. Other fields of bird strike design already use analytical formulations to predict critical birds strike locations on turbofan blades. Studies like Sinha et al.'s 2011 journal article [60] utilise transient analytical models to allow the blade designer to identify critical impact locations for peak dynamic loading conditions. There is also Yu et. al.'s 2019 article [68], that demonstrates how analytical bird strike models can be utilized to determine critical impact locations on leading edges.

Both Sinha et al. [60] and Yu et al. [68] base part of their analytical load prediction model on Willbeck and Barber's work [66, 14]. Hence, this research aims to utilise the same bird strike load prediction models to allow the analysis of bird strike intensity over large arbitrary bodies. Such analysis may allow the OEM to showcase critical bird strike locations to regulatory bodies and to reliably identify the worst impact scenarios that are expected during operation. With this in mind, the following research objective can be formulated:

The research objective is to utilise decoupled analytical bird strike load models to devise a methodology that predicts bird strike intensity for arbitrary aircraft concepts, dependent on their flight path.

3 Methodology

The following sections elaborate on all models and procedures used for the research methodology. Additionally, the final methodology.

Section 3.1 introduces the different phases of a bird strike impact. It is followed by section 3.2, which breaks down how bird strike duration and load can be predicted. Section 3.3 describes how impact scenarios are defined for arbitrary shapes and flight paths. Lastly, section 3.4 summarises how the previously discussed methods are defined to create bird strike intensity maps.

3.1. Introduction to Bird Strike Physics

Most publications categorise bird strikes as a soft body impact. However, as mentioned by S. Abrate in his 2015 paper [5], there exists no universally used definition. Nevertheless, Hedayati et al. [37] use a similar definition as Abrate in their 2016 book on bird strike. Both describe soft body impact as a collision in which the strength of the projectile greatly subceeds the strength of the target. Abrate adds that the stresses occurring during the impact substantially exceed the strength of the projectile, whilst being less than the target's strength. However, this addition stands in contrast to actual bird strike, as it often leads to permanent damage to structures. The combination of simultaneous interactive high deformations and high strain rates make bird strike a challenging non-linear phenomenon to model. Additionally, bird geometry may vary vastly. Furthermore, impacts may occur over a large variety of structures and materials, requiring new derivations and complicated procedures to be repeated if analytical formulations are used. These challenges lead to the almost exclusive use of numerical modelling methods when analysing bird strike. [5, 37, 38]

Numerical methods, on the other hand, have their unique challenges. Most meta-studies or books on bird strike agree that there exists no industry standard for bird strike modelling methods. The four most used methods are: Lagrangian, Eulerian, arbitrary Lagrangian-Eulerian (ALE), and Smoothed Particles Hydrodynamics (SPH). The majority of current publications on this topic are focused and the ALE and SPH method [37, 38, 43, 58].

Eulerian methods are well-known in the field of computational fluid dynamics (CFD). The main difference to Lagrangian methods is that the mesh is fixed in space and not attached to the bird mass. ALE is a variant in which the mesh is resized to only cover the area that contains bird mass, to decrease computational cost. In any case, the changing domain size further increases the complexity of the programme, making the implementation of ALE models very difficult. Additionally, mass leakage may occur between elements. Lavoie et al. [44] report mass losses of up to 25% in their 2009 study. These modelling methods are also less stable than purely Lagrangian methods [37, 38, 54].

SPH models are mesh-less Lagrangian methods that utilise equations of motions similar to FEM models, but particle forces and states are determined by kernel smoothing functions. These kernel functions depend on the surrounding particles within a certain radius. The SPH method allows for an easier integration with other lagragian methods, like FEM, when compared to Eulerian methods. This means that interaction between bird mass and impactor body is easier to determine than in Eularian methods. Additionally, fewer elements are needed, making it less computationally expensive than ALE models, for instance.

Besides their ability to give order of magnitude estimation of impacts, analytical models are also great at showcasing the physics behind bird impact. According to Wilbeck, a bird impact can be split into four distinguished phases. Each phase is depicted in Figure 3.1. The first phase can be seen in the upper left corner. The impactor just made contact with the target, leading to an abrupt deceleration of the contacting mass, thus resulting in a shock wave that travels opposite to the impact direction up the projectile body. During this phase, the pressure in the shocked region peaks to the so-called Hugoniot pressure. The pressure difference between the shocked region and the outer free surface of the projectile leads to a radial outwards acceleration of the impactor mass. This forms release shock waves as seen in the upper right corner. These release waves travel towards the center, reducing the pressure and terminating the Hugoniot pressure; making it very short lasting. The release waves reflect the initial shock wave. They are bouncy between the phase touching the target and the initial shock wave, further reducing the pressure until equilibrium is reached, as seen in the third stage. During this steady state, the pressure remains constant and the material is further spreading. A typical pressure-time graph can be seen in Figure 3.2. A short peak can be observed as well as a period of almost constant pressure [38, 37, 66].

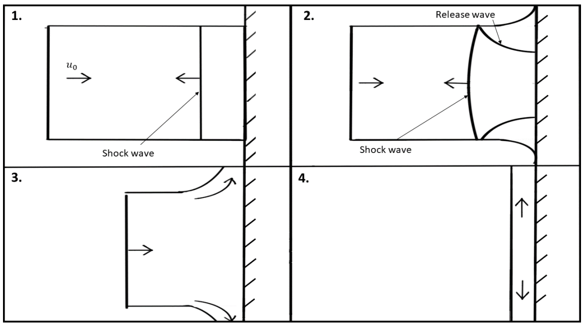

Figure 3.1: Illustration of Soft Body impact on rigid surface

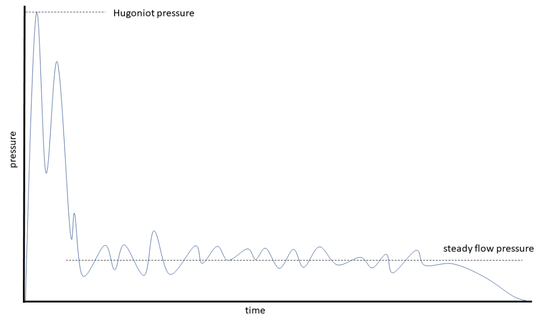

Figure 3.2: Typical pressure vs. time

3.2. Bird Strike Load Models

The following subsections will introduce two analytical load prediction models that assume a flat and rigid impacted surface.

Section 3.2.1 elaborates how the timing between different impact phases is determined. It follows subsections 3.2.2 and 3.2.3 that demonstrate Wilbeck [66] and Barber's [14] 1978 models for bird strike load prediction. Finally, subsection 3.2.4 presents the most used bird material model as well as commonly used equations of state.

3.2.1. Timing

Before the pressure history can be known, it is important to understand how the duration of the different impact phases are determined. All of the following equations and theories are taken from Wilbeck's 1978 paper [66] on the impact behaviour of low-strength projectiles.

The total impact duration t_D can be determined with the so called squash time, by calculating the time the projectile would need to travel its own length. This can be done by dividing the impactor length L by the impact speed u_0 as seen in Equation 3.1.

$$t_D = L/u_0 \tag{3.1}$$

To determine the duration of the peak pressure and steady state period, a closer look at the shock dissipation is necessary. Figure 3.3 offers a detailed sketch of the different shockwaves interacting and the resulting release regime. The black regions in Figure 3.3 a, b represent the high-pressure region that follows the initial shock wave. These regions generate an abrupt outwards movement of the bird mass due to the high-pressure gradient between the free surfaces of the impactor body and the shocked area. Figure 3.3 b.) depicts the outwards movement and the forming of release waves at the outer corners of the projectile. Wilbeck assumes the peak pressure period to be over once both release waves reach point B as seen in Figure 3.3 c.). As the release waves catch up with the initial shock wave, the shocked region is weakened, severely reducing its pressure and velocity. The release waves keep on reflecting until equilibrium is reached and the steady state phase is reached.

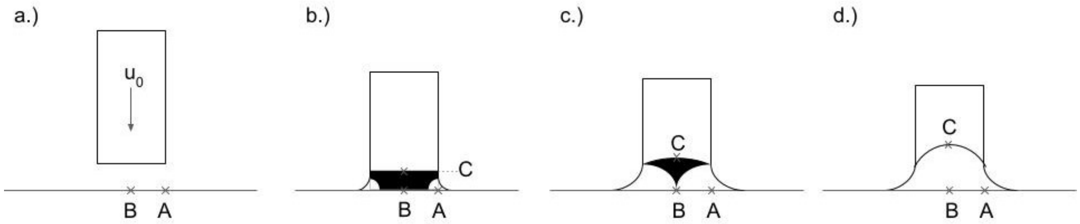

Figure 3.3: Release Regime [66]

Equation 3.3 determines the time the release waves require to meet at point B, where a is the projectile radius and c_r for the release wave speed. According to Wilbeck, the release wave speed can be assumed to be equal to the speed of sound in the shocked region. The speed of sound may be assumed to be equal to the gradient of the isentropic pressure-density curve at the Hugoniot pressure, as seen in Equation 3.2. One may obtain such gradient by differentiating an equation of state (EOS).

$$c_r^2 = \left(\frac{dP}{d\rho}\right)_{P_H} \quad (3.2) \qquad t_B = \frac{a}{c_r} \quad (3.3)$$

Wilbeck assumes that the steady state is reached once the release waves reach the initial shock wave, dissipating the shock region. This happens once bot waves reach point C as seen in Figure 3.3 d.). Equation 3.4 marks the starting time of the steady state. For projectiles that have a lower aspect ratio, this state may never be reached, as the release waves are not catching up to the shock wave before the impact is terminated. Equation 3.5 expresses the critical aspect ratio $(L/D)_c$ as a function of the impact velocity. If the aspect ratio of the projectile is smaller than the critical ratio, then no steady state is reached. The derivation of both equations can be found in appendix A.1.

$$t_c = \frac{a}{\sqrt{c_r^2 - (u_s - u_0)^2}} \quad (3.4) \qquad (L/D)_C = \frac{u_s}{2\sqrt{c_r^2 - (u_s - u_0)^2}} \quad (3.5)$$

Wilbeck determines the shock velocity using the ”linear-Hugoniot” seen in Equation 3.6, which contains the speed of sound of the impactor material, c_0, the impact speed, u_0 and a constant, k. According to Wilbeck, the constant should be equal to 2.

$$u_s = c_0 + u_0 \cdot k \quad (3.6)$$

To take into account changes in impact angle, one can adjust all dimensions. For example, an inclined impactor projects an elliptical area onto the target. To determine the peak pressure period, one may replace a with half the major axis of the ellipse. Similarly, the length of the projectile can be adjusted. However, the correct velocity needs to be taken into account. To determine the squash time, only the vertical portion of the velocity is needed. Figure 3.4 depicts the difference between yawed and oblique impact.

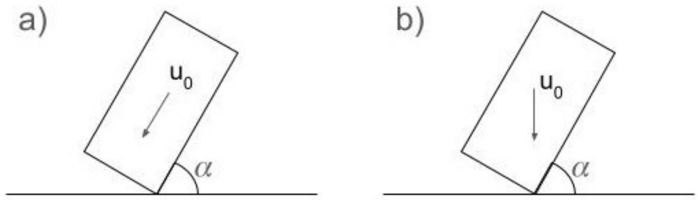

Figure 3.4: Sketch showing the difference between oblique impact (a) and yawed (b)

3.2.2. Willbeck

The load prediction models introduced in this subsection are in their entirety taken from Wilbeck's report published in 1978 [66]. Wilbeck uses his models to predict the initial peak pressure, as well as a pressure distribution during the steady state phase.

The peak pressure can be defined by Equation 3.7 and 3.7. Equation 3.7 uses the speed of sound of the material, c_0, to approximate the shock propagation velocity, whilst Equation 3.8 uses the approximation given by the linear Hugoniot seen in Equation 3.6. The derivation of of both equations can be found in the appendix A.2. In the case of an oblique impact, only the normal velocity is taken into account. Therefore, the peak pressure changes with the sin of the impact angle, α.

$$P_H = \rho \cdot c_0 \cdot u_0 \quad (3.7) \qquad P_H = \rho \cdot u_s \cdot u_0 \quad (3.8)$$

Assuming that the force during the steady phase is impacted and that the projectile will transfer all its momentum into the structure, it is possible to determine the total force exerted, as well as the average pressure. A more detailed derivation can be found in appendix A.2. It can be assumed that only the normal component of the total momentum will be transferred. Hence, similarly to the Hugoniot pressure, the total force exerted changes with the sin of the impact angle α for oblique impacts.

$$F_a = \rho \cdot A \cdot u_0^2 \quad (3.9) \qquad P_a = \rho \cdot u_0^2 \quad (3.10)$$

Assuming the shock waves are sufficiently weakened once the release waves meet the shock wave, it is possible to presume that streamlines form throughout the bird. Using this assumption, it is possible to derive a formulation for the stagnation pressure as seen in Equation 3.11. Equation 3.11 is only valid when incompressibility is assumed. The stagnation point of a compressible material will always be higher. The more detailed derivation is shown in appendix A.2.

$$P_s = \frac{1}{2} \cdot \rho \cdot u_0^2 \tag{3.11}$$

Wilbeck introduces two formulations for the pressure distribution during the steady state phase. Both need to fulfil the following criteria: Firstly, the pressure at the origin needs to be equal to the stagnation point pressure, P_s. Secondly, the pressure needs to approach 0 asymptotically as the distance to the center, r, approaches infinity. Lastly, the total applied force needs to be equal to the force calculated with Equation 3.9. Both formulations are originally synthesised to describe the pressure distribution of a jet of water hitting a flat rigid plate. Equation 3.12 is the Banks & Chandrasekhara [13] formulation. Leach & Walker's formulation [46] can be found in Equation 3.13. It is important to note that Leach & Walker's formulations as found in Wilbeck's report [66] differs from the formulation of the original source. Wilbeck's version, in any case, does not satisfy the criteria. Therefore, it is assumed that the original is the correct version.

The constants values of ξ_1 and ξ_2 are given by Wilbeck. ξ_1 is equal to 0.5 and ξ_2 to 2.58. As the formulation is derived for incompressible flow, ρ stays constant.

$$P = \frac{1}{2}\rho u_0^2 e^{-\xi_1(\frac{r}{a})^2} \quad (3.12) \qquad P = \frac{1}{2}\rho u_0^2 \left\{ 1 - 3\left(\frac{r}{\zeta_2 a}\right)^2 + 2\left(\frac{r}{\zeta_2 a}\right)^3 \right\} \quad (3.13)$$

3.2.3. Barber

The model introduced in this subsection was published in the same year as Wilbeck's model and he was one of the publishing authors. Barber et al. published the paper [14] predicting the loads during the steady state phase utilizing 3-dimensional potential flow theory. Similar to Equation 3.12, the bird is assumed to be a steady jet of water hitting a flat rigid plate. The flow is assumed to be incompressible and irrotational so that the Laplace equation seen in Equation 3.14 can be used as a governing equation.

$$\nabla^2 \varphi = \frac{\partial^2 \varphi}{\partial x^2} + \frac{\partial^2 \varphi}{\partial y^2} + \frac{\partial^2 \varphi}{\partial z^2} \tag{3.14}$$

A solution is found by superpositioning two elemental solutions of the Laplace equation, one of the uniform flow of a round duct onto the place, and the second one is a uniform distribution of planar sources over the elliptical impact area of the flat plate. Figure 3.5 offers a clear overview of the used coordinate system, as well as a visual representation of both flows.

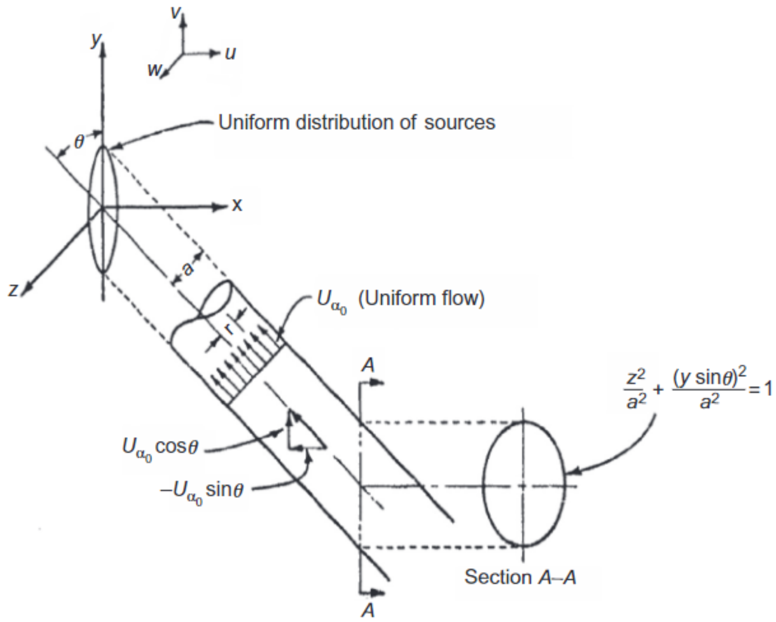

Figure 3.5: Sketch Oblique Impact Potential Flow Model [14]

There exists no closed form solution to determine the flow over the elliptical bound solution defined by Equation 3.15. However, there exists a solution for definite integration over square elements. Therefore, the area needs to be discretized into squares elements as seen in Figure 3.6. Each element is assumed to be within bounds if its center is within the ellipse, as marked by the orange dots.

$$1 = \frac{z^2}{a^2} + \frac{\left(y \cdot sin(\theta)\right)^2}{a^2} \tag{3.15}$$

Equation 3.16 to 3.18 are expressions originally developed by Kellogg in 1929 [40] that can be used to compute the velocity field induced by the planar sources. The r terms are defined in Equation 3.19. It is important to note that the term for r_3 is defined wrongly in Hedayati et al.'s book [37]. Each element has uniform sources located at their corners, (η_1, ζ_1), (η_1, ζ_2), (η_2, ζ_1) and (η_2, ζ_2). Equation 3.20 defines the strength of the sources q'' such, that the velocity in u at any point of the z-y plane is equal to zero.

$$\begin{aligned} u(x, y, z) =& \frac{q''}{4\pi} \left\{ \tan^{-1} \frac{(z - \xi_2)(y - \eta_2)}{x r_3} + \tan^{-1} \frac{(z - \xi_1)(y - \eta_1)}{x r_1} \right. \\ & \left. - \tan^{-1} \frac{(z - \xi_1)(y - \eta_1)}{x r_2} - \tan^{-1} \frac{(z - \xi_2)(y - \eta_1)}{x r_4} \right\} \end{aligned} \tag{3.16}$$

$$v(x, y, z) = \frac{q''}{4\pi} \ln \left\{ \frac{[r_3 + (\xi_2 - z)]\,[r_1 + (\xi_1 - z)]}{[r_4 + (\xi_2 - z)]\,[r_2 + (\xi_1 - z)]} \right\} \tag{3.17}$$

$$w(x, y, z) = \frac{q''}{4\pi} \ln \left\{ \frac{[r_3 + (\eta_2 - y)]\,[r_1 + (\eta_1 - y)]}{[r_2 + (\eta_2 - y)]\,[r_4 + (\eta_1 - y)]} \right\} \tag{3.18}$$

$$\begin{aligned} r_1 &= \sqrt{x^2 + (y - \eta_1)^2 + (z - \xi_1)^2} \\ r_2 &= \sqrt{x^2 + (y - \eta_2)^2 + (z - \xi_1)^2} \\ r_3 &= \sqrt{x^2 + (y - \eta_2)^2 + (z - \xi_2)^2} \\ r_4 &= \sqrt{x^2 + (y - \eta_1)^2 + (z - \xi_2)^2} \end{aligned} \tag{3.19}$$

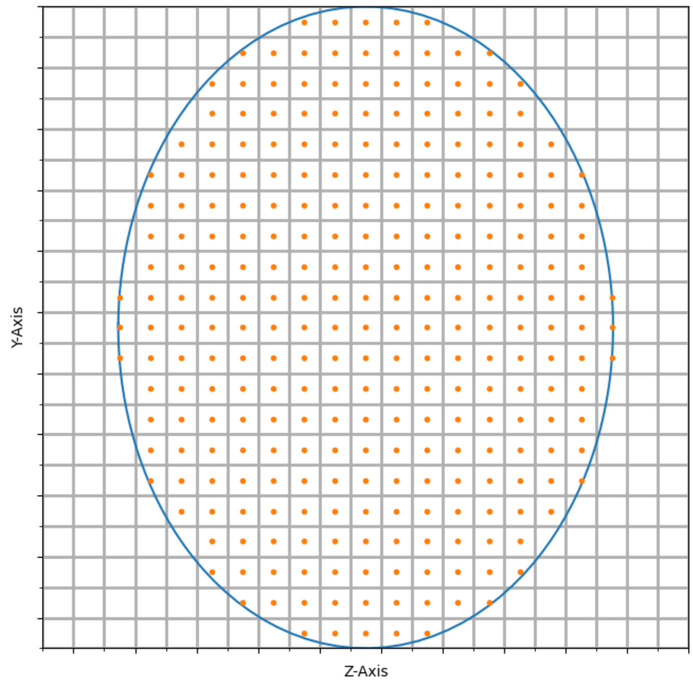

Figure 3.6: Dicretization of boundary area

$$q'' = 2U_\infty sin(\theta) \tag{3.20}$$

The flow velocity in y and z direction can be defined at any point by Equation 3.21 and 3.22. The U velocity is 0 at any point on the y-z plane, therefore no equation is needed. $V_k(0,y,z)$ is equal to $v(0,y,z)$ from Equation 3.17 of element k. The 1st term $U_\infty cos(\theta)$ is the addition of the uniform flow of the round duct in the y direction. Equation 3.22 worked similarly, although the free stream does not contribute to the z direction. The formulation found by Barber [14] and Hedayati [37] includes the $\frac{q''}{4\pi}$ term in these equations.

$$V(0,y,z) = U_\infty cos(\theta) - \sum_k V_k(0,y,z) \tag{3.21}$$

$$W(0,y,z) = \sum_k W_k(0,y,z) \tag{3.22}$$

The pressure coefficient can be calculated from the velocities as seen by Equation 3.23. Barber [14] and Hedayati [37] both use a wrong definition of c_p, but Barber uses the correct one in his original code. The derivation of Equation 3.23 can be found in appendix B.1.

$$c_p = 1 - \frac{V^2 + W^2}{U_\infty^2} \tag{3.23}$$

$$P = \frac{1}{2}\rho U_\infty^2 c_p \tag{3.24}$$

3.2.4. Equations of State

Equations of state (EOS) are used to describe the correlation between different state variables. They often describe the relationship between density or volume, internal energy, temperature and pressure. One of the most commonly known EOS is the ideal gas law. Wilbeck, as well as Barber, require an EOS to determine the release wave velocity described by Equation 3.2. The bird mass during impact is assumed to be liquid, hence the EOS for water is commonly used. Since there exists no analytically derived EOS, semi-empirical equations are used to approximate the liquid's behaviour. Sometimes, tabular EOS based on measurements are used as well. It follows an assortment of often used EOS.

Linear EOS

The simplest EOS is the linear EOS seen in Equation 3.25. P is the pressure, K is the bulk module, ρ the material density and ρ_0 the initial material density. This equation and the value K are taken from Guida et al.'s 2013 paper [36].

$$P = K\left(\frac{\rho}{\rho_0} - 1\right) \tag{3.25}$$

Table 3.1: Values for Linear EOS

Scource	K [MPa]
[36]	2200

Murnhagan EOS

The Murnhagan or Tait's equation seen in eq. 3.26 is another EOS that is used in bird impact studies. P_0 denotes the reference pressure, ρ the material density, ρ_0 the initial material density, B and γ are material constants. As seen in Table 3.2, most sources give fixed values for the material constants. Abrate [5], however, relates B to the wave velocity c for values $\rho > \rho_0$ as seen in Equation 3.27. The resulting variables can be found in Table 3.2 [38, 37, 47, 5].

$$P = P_0 + B\left(\left(\frac{\rho}{\rho_0}\right)^{\gamma} - 1\right) \tag{3.26}$$

$$B = \rho_0 \frac{c^2}{\gamma} \tag{3.27}$$

Table 3.2: Values for Murnhagan's EOS

Scource	B [MPa]	γ [-]	P_0 [Pa]
[38, 37, 47]	128	7.98	0
[5]	2.984 / $\rho_0 \frac{c2}{\gamma}$	7.15	0

Polynomial EOS

According to Heimb's 2011 meta-analyses [38], the polynomial EOS is the most often used EOS for bird impact. Equation 3.28 depicts the EOS. Most variables are set to 0, so that the internal energy E_i is cancelled out of the equation. The remaining constants are listed in Table 3.3, including values for different porosities. For this equation relative density is used, as described by Equation 3.29 [38, 5].

$$P = c_0 + c_1\mu + c_2\mu^2 + c_3\mu^3 + (c_4 + c_5\mu + c_6\mu^2)E_i \tag{3.28}$$

$$\mu = \frac{\rho}{\rho_0} - 1 \tag{3.29}$$

Table 3.3: Values for Polynomial EOS, $c_0 = c_4 = c_5 = c_6 = 0$

	0% Porosity			10% Porosity			15% Porosity		
Sources	c_1 [MPa]	c_2 [MPa]	c_3 [MPa]	c_1 [MPa]	c_2 [MPa]	c_3 [MPa]	c_1 [MPa]	c_2 [MPa]	c_3 [MPa]
[38]	2250	0	0	511.7	-8224	55, 150	748.4	-9622.1	36, 120
[5]	2060	6160	10, 300	28	-85	35, 000	6.9	-3180	31, 000

3.3. Bird Strike Scenarios

To estimate the bird strike intensity with the previously described models, several things need to be known. Firstly, the composition of the bird including mass, geometry and material properties such as speed of sound and density. Secondly, the impact scenario comprised of the impact angle and velocity. During operation, bird composition may vary vastly from impact to impact. However, the certification standards presented in section 2.2 provide a standard bird mass. Using these compositions lends itself when one wants to create a comprehensive bird strike intensity map. Table 3.4 lists the standard bird composition, used to this day in most bird strike tests [66, 37].

Table 3.4: Standart Bird parameters [66, 37]

ρ_0 [kg/m^3]	c_0 [m/s]	m [kg]	L/D [-]
950	1482.9	1.81	2

The only parameters missing are velocity and impact angle. Velocity needs a magnitude as well as a direction. The magnitude may be chosen to be dictated by the regulations summarized in subsection 2.2.3. Nevertheless, the angle relative to the aircraft is not defined. It is also possible to use a typical flight path profile containing angles of attack and the associated speeds.

The impact angle is a function of the velocity vector and the point of interest on the aircraft surface. To generate the angle, the surface is discretized. A common file format to safe shapes is the stl file. STL is an abbreviation and originally stands for stereolithography, a commonly used 3D-printing technology. However, it is also often seen as Standard Triangle Language or Standard Tessellation Language. As suggested by the name, stl files save the shape in the form of triangles. The vortexes of each element are saved in a cartesian coordinate system, together with a unit normal vector pointing outwards.

Figure 3.7 illustrates how the stl file is used to gather all parameters needed to calculate a bird strike load. On the left of the figure, the discretized geometry can be seen. As all triangles are flat, all points within the element will give the same result. Therefore, impact scenarios need to be determined for each element. Element i is marked red, and the velocity vector is represented by the red arrow. The middle of Figure 3.7 depicts element i including the velocity vector and its unit vector, n_i. The cosine between two vectors can be calculated using Equation 3.30. Thus, the impact angle α can be computed by subtracting the angle between the two vectors from the right angle, as seen in Equation 3.31. As all normal vectors point outwards of the shape, negative impact angles denote that the impact is impossible. Pyvista, the python module used to read stl files, contains ray tracing functions, making it possible to further eliminate elements that are shielded. The final step shown in Figure 3.7 denotes that all parameters are known to calculate the impact loads for each hit element.

$$cos(\beta) = \frac{\vec{u_0}.\vec{n_i}}{|n_i|\,|u_0|} \qquad (3.30)$$

$$\alpha = \frac{\pi}{2} - \beta \qquad (3.31)$$

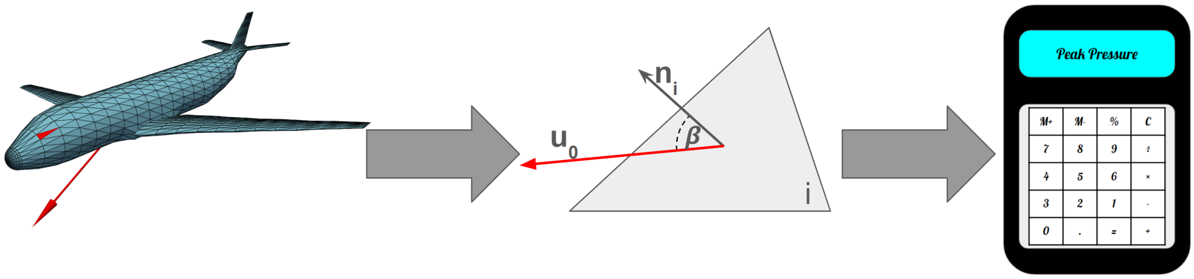

Figure 3.7: STL file processing

3.4. Methodology Composition

To create a methodology that satisfies the research objective stated in section 2.3, several criteria need to be met. The methodology needs to have a sufficiently high resolution to distinguish different areas. It also needs to be able to establish a hierarchy of impacts, to be able to distinguish the most intense impact per area. Lastly, it needs to be universally applicable, so that a large variety of aircraft can be evaluated.

The impact scenarios can be distinguished as per the methodology introduced in section 3.3. Therefore, the resolution is defined by the resolution of the stl file. If a CAD model of the outer mould of the aircraft is available, the resolution is freely selectable, as most CAD programs can tesselate the model in any desired resolution.

To establish a hierarchy between impacts, a single parameter needs to be chosen to define impact intensity. Section 3.2 introduces the bird models. Both Barber and Wilbeck's model can be used to create average pressure histories for each impact. Parameters of interest can be deduced from this data. The most promising parameters are the total impulse, j_{tot} and the Hugoniot pressure, P_H. Other parameters like the normal component of the kinetic energy are already expressed in the peak pressure. What parameter is more consequential will be further analysed in chapter 4.

The universal applicability of the methodology is already given, as the choice of flight path vector and a CAD model of the aircraft provides all the means necessary to execute the methodology.

Figure 3.8 depicts the proposed flow of the methodology. Each orange box represents a program. The stl file is generated by using 3DEXPERIENCE, as it is the CAD program made available by the faculty. However, any CAD program may be used. Each white box represents the inputs needed for the methodology. The lists within the box specify the input parameters. Due to ease of use and the familiarity of the author, Python was chosen as the programming language to execute the methodology.

As part of the thesis, a publicly accessible Python package has been created containing Wilbeck and Barber's models described in section 3.2. The package is available under : `https://pypi.org/project/birdpressure/`. The "Impact Scenario Generator" script utilises a package called *pyvista* to perform all operations on the stl, as well as the rendering. The code generates bird models for each element and each flight phase. This allows the program to generate a library containing all possible bird strike scenarios experienced by each element. By assigning a chosen intensity parameter to each element, it is possible to create heat maps. It is also possible to post-process the data to showcase the worst possible impact per element.

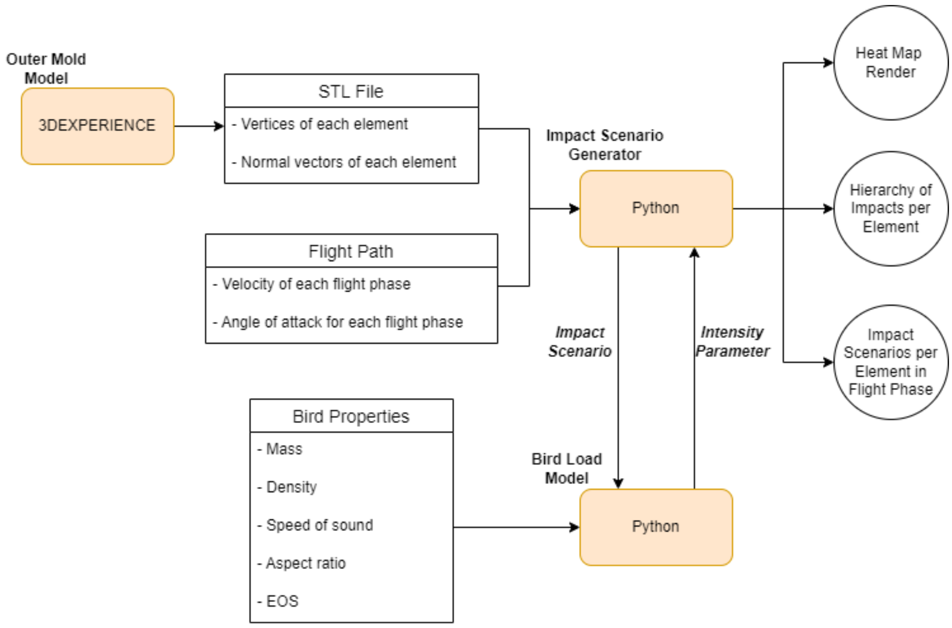

Figure 3.8: Methodology Flow chart

Figure 3.9 depicts a possible use of the methodology. To showcase the universal applicability, a cow-shaped example file of the *pyvista* package was chosen. The top part of the picture showcases the worst impacts on the geometry, based on Hugoniot pressure. Underneath, three smaller renders can be seen showcasing the three different phases; run, jump and land. The flight path input is summarised in Table 3.5. The opaque elements are elements that have a negative impact angle or elements that are shielded.

When examining the three phases, the impact of the velocity vector becomes apparent. This is expressed by the change in expected peak pressure values, as well as the change in hit areas. Further processing of the gained data may present further insights. For instance, to compare hit area per flight phase, one could also determine what area percentage of the worst case render belongs to what phase. Moreover, it is possible to compare the worst impact scenarios to the scenario required by the regulations summarized in subsection 2.2.3.

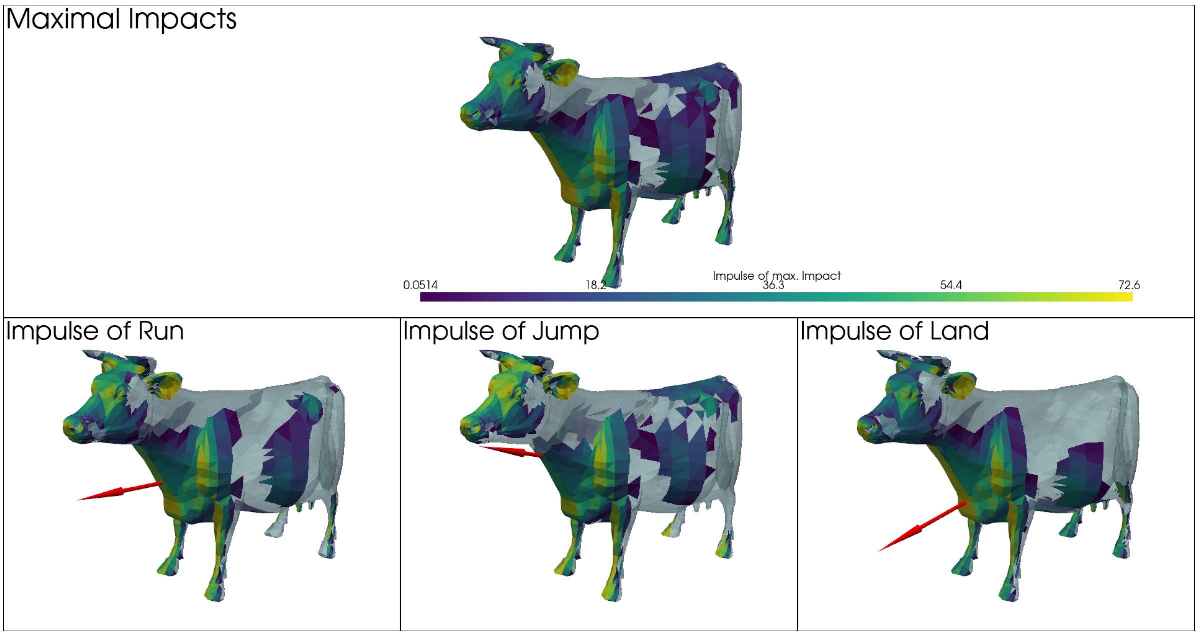

Figure 3.9: Demonstration of methodology based on jumping cow

Table 3.5: Flightpath input

	Angle of attack [deg]	Speed [m/s]
Run	0	20
Jump	-15	30
Land	15	40

3.5. Methodology Limitations

The proposed methodology has limitations that are inherent to its design. Both the processing of the stl file and the load models have their drawbacks.

Firstly, hit and not hit areas are solely determined by the line of sight of the flight path vectors. The airflow is not taken into account. In reality, there are low-pressure areas like the inlet of engines that tend to suck in debris as mentioned by Hedayati et al. [37]. These effects are not taken into consideration by the method herein proposed.

Secondly, the load model. The analytical models used in the methodology are decoupled, therefore they always assume a rigid and flat structure. However, the impact of bird-structure interaction has been mentioned as early as 1980 in West et al.'s report [65]. West et al. state that the analytical load models are insufficient to design structures with a high level of confidence.

There exist limitations based on the definition of the bird impact and on how the load models are utilized within the methodology.

The impact location may be located at a part of the aircraft that is smaller than the bird itself, as depicted by Figure 3.10 and 3.11. When comparing both impacts, the impact of Figure 3.10 would be determined to be the more intense impact, due to it being a normal impact. However, as indicated by the red area, the majority of the bird mass would not directly impact the structure.

Additionally, smaller radii pose a challenge. The methodology assumes flat surfaces, the smaller the radius the bigger the difference between the assumption and the hit geometry.

Yu et al. [68] circumvents this discrepancy by discretizing the bird, determining a Hugoniot pressure and total impulse for each element and individual impact angle. However, the addition of such features may result in a methodology that is too time-intensive.

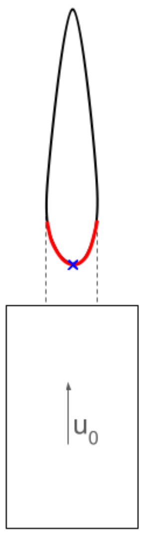

Figure 3.10: Normal impact on small radius

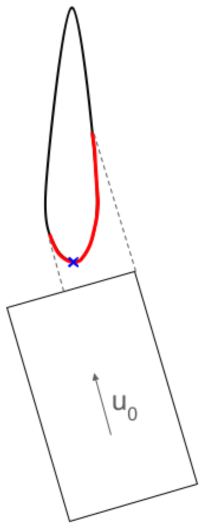

Figure 3.11: Oblique impact on small radius

4

Verification & Analyses of Methodology

This chapter offers a collection of tests created to verify the results methodology, as we as compelling arguments for the advantages the methodology offers for the bird strike design and certification process. The results of said tests are presented and discussed.

Starting with section 4.1, which motivates the choice of EOS used for all analytical models. Section 4.2 contains tests chosen to validate the bird strike load models. The following section, 4.3, compares the results of the methodology to Chen et al.'s study [20] on bird impact on the Flying-V. Finally, section 4.4 will demonstrate different possible uses of the methodology.

4.1. Equation of State

This section showcases the impact different equations of state have on the analytical bird strike prediction models.

Figure 4.1 depicts the shock velocity, u_s, as well as the release wave velocity, c_r, for different equations of state over a range of impact velocities u_0.

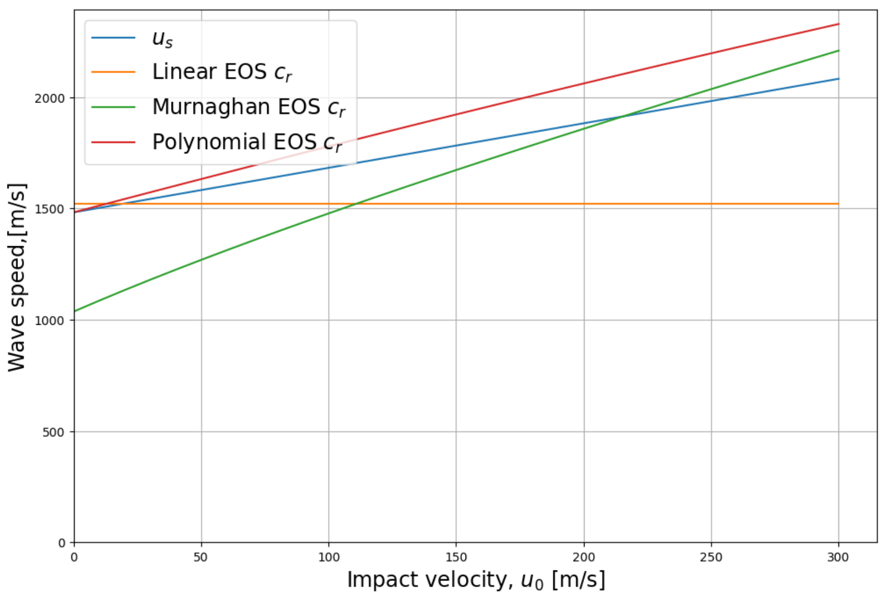

Figure 4.1: Wave velocities for shock wave and release waves for different EOS

EOS are used to determine the release wave velocity, c_r, as defined by Equation 3.2. The release wave velocity is needed to determine the peak pressure duration as well as the timing of the steady state period as seen in Equation 3.3 and 3.4. It is also used to determine the critical aspect ratio (Equation 3.5), marking the geometry from which on steady state can be reached. Section 3.2.4 defines the different equations of state.

For the aforementioned equations to work, the release wave velocity must be higher than the shock wave velocity subtracted by the impact velocity, as seen in 4.1. If that is not the case, the formulations fail due to a negative value under a root.

$$c_r \geq u_s - u_0 \tag{4.1}$$

When inspecting Figure 4.1, it becomes apparent that only the polynomial EOS results consistently in release wave speeds that are higher than the shock wave speeds. Therefore, all models utilize the polynomial equation of state, ensuring results over the whole range of impact velocities.

4.2. Load Prediction Models Verification

This subsection contains the validation of the *birdpressure* module and the motivation of the preferred bird strike intensity parameter.

The data used for the validation was provided by Post, based on the SPH model created for his 2024 thesis [56]. Table 3.4 provides the bird parameters used in all of the following analyses. The provided data set provided time-stamped pressure and force data that was averaged over the impact area. There are two impact velocities of 90 and 180 m/s with oblique impact angles ranging from 90 to 40 deg in 10-degree steps. Corresponding Wilbeck and Barber models were created for each scenario. Both models have two versions, one taking into account an area change due to the elliptical cross-section, the other not. The raw data is further processed to create singular values that can be compared to the results of the analytical models.

The SPH data is very noisy, therefore some signal processing is advised to evaluate the data better. Post refers to Airoldi et al's 2006 study [8] in which a fourth-order Butterwort filter is suggested. The filter acts like a low-pass filter, and a cut-off frequency of 50kHz is suggested.

Firstly, t_D is determined as seen in Equation 3.1. The Hugoniot pressure/force is equal to the highest recorder pressure/force within 0 and $1/3t_D$. It is assumed that the steady state period is reached between $1/3t_D$ and t_D. The peak pressure duration is determined by finding the minimum force occurring between the peak force (F_H) and the force at $1/3t_D$. Both the steady state pressure (F_s) and force (F_s) are calculated by taking the average values between $1/3t_D$ and t_D. Finally, t_D is redefined as the time at which the force reaches 10% of the previously defined steady state force. The total impulse is calculated by determining the area under the force-time curve, using the trapezoid rule.

4.2.1. Results

This subsection contains all results needed to motivate the conclusion of the analysis. Often, figures of a select few impact scenarios are shown, and the totality of the data can be found in the dataset [16].

The results are represented in two groups. Firstly, different scenarios are compared based on the pressure and force history as well as a multitude of parameters. Secondly, the most interesting parameters are compared based on their change between scenarios.

Scenario Data Comparison

The following figures depict two types of force graphs generated from the above-described data. Figure 4.2 and 4.3 showcase how well the processed values of F_H, F_s, t_b and t_D fit the raw and filtered data. Further, Figure 4.4 and 4.5 contain the SPH data and the force history created by the analytical models.

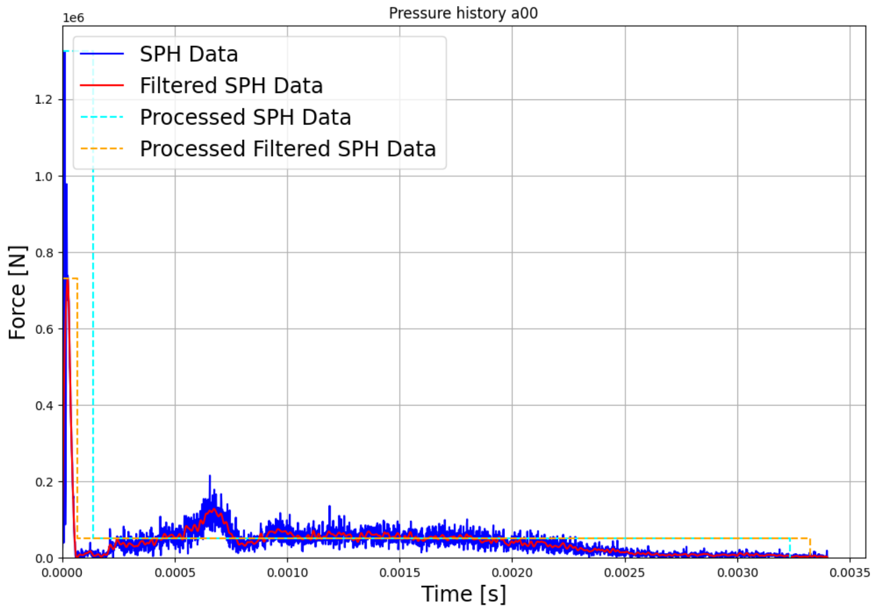

Figure 4.2: Processed force data comparison, u_0 = 90 m/s, α = 90 deg

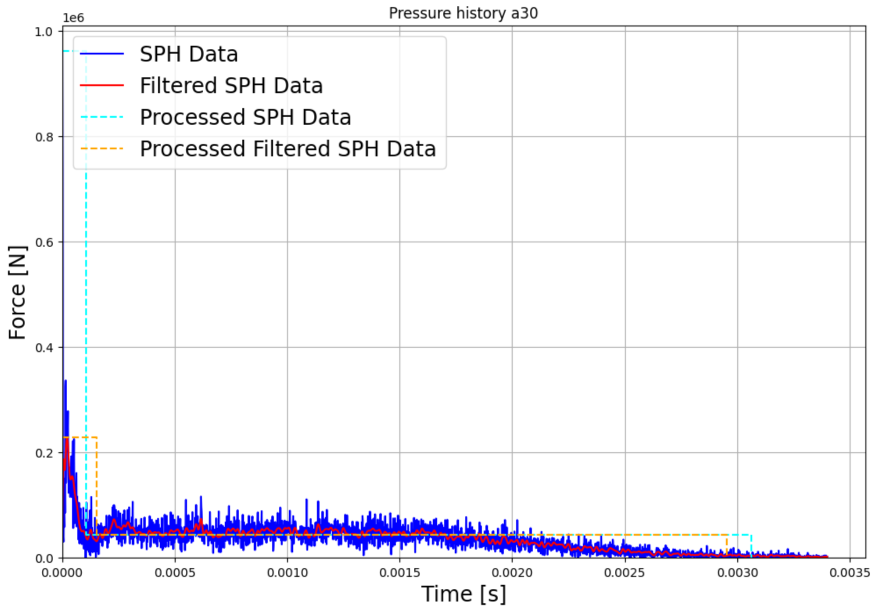

Figure 4.3: Processed force data comparison, u_0 = 90 m/s, α = 60 deg

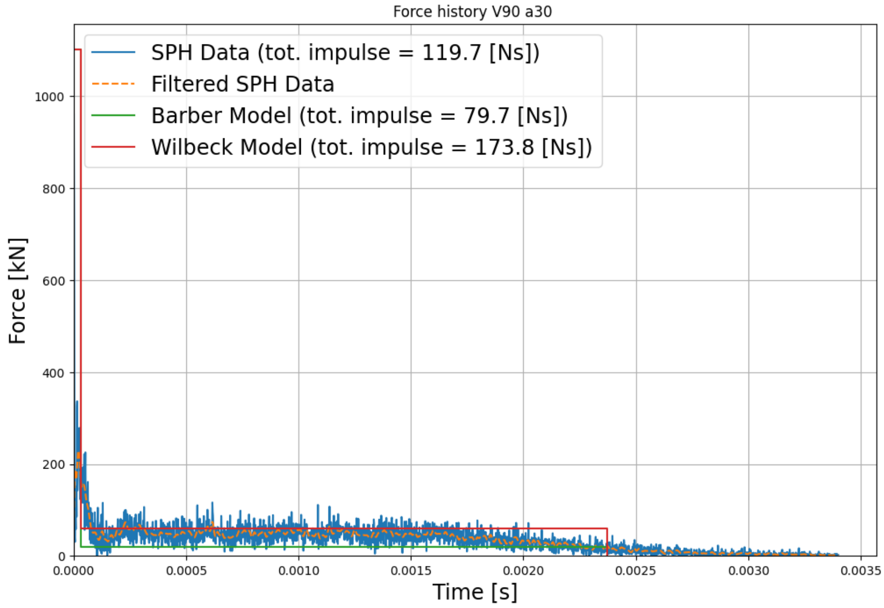

Figure 4.4: Comparison analytical models to SPH force data, u_0 = 90 m/s, α = 90 deg

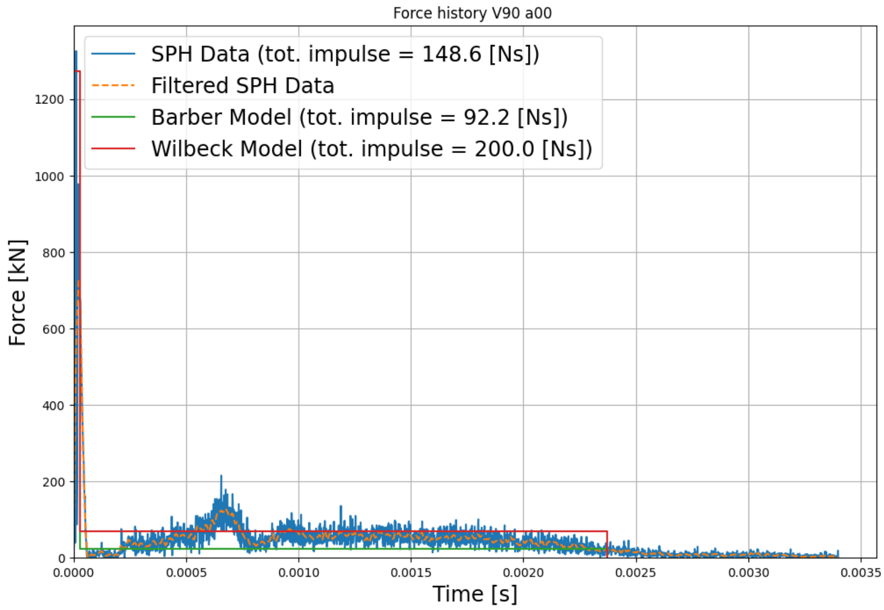

Figure 4.5: Comparison analytical models to SPH force data, u_0 = 90 m/s, α = 60 deg

The following figures are divided similarly as above. Figure 4.6 visualizes the processed parameters and plots them together with the SPH data. Further, Figure 4.7 allows the comparison between SPH pressure data and the analytical model.

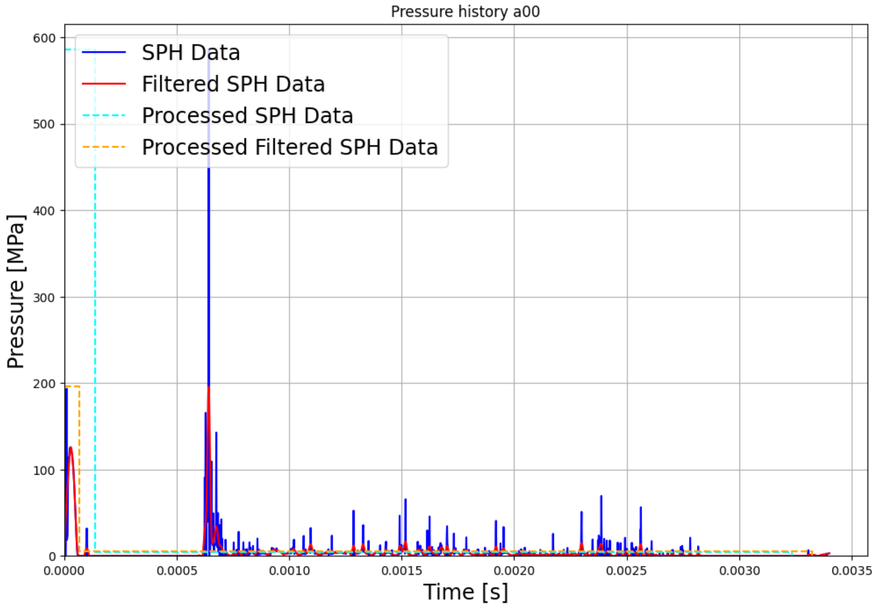

Figure 4.6: Processed pressure data comparison, u_0 = 90 m/s, α = 90 deg

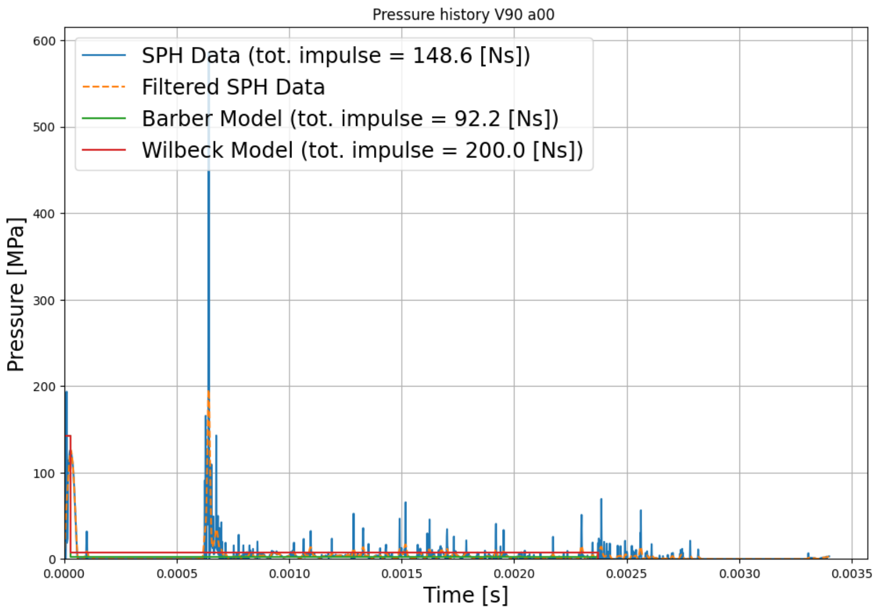

Figure 4.7: Comparison analytical models to SPH pressure data, u_0 = 90 m/s, α = 90 deg

The here presented tables offer an overview of all results per impact scenario. Table 4.1 contains the results for a 90 m/s impact with a 90 degree impact angle. To keep the tables consistent with the figures, Table 4.2 consists of data for an oblique impact of 90 m/s with a 60-degree angle.

Table 4.1: Processing results, u_0 = 90 m/s, α = 90 deg

	total impulse [Ns]	P_H [Mpa]	P_s [Mpa]	F_H_av [N]	F_s_av [N]	t_b [ms]	t_D [ms]
SPH_unfiltered	148.56	585.64	4.68	1325176	51155	0.138	3.23
SPH_filtered	148.52	195.72	4.98	729991	50969	0.067	3.335
Barber	92.17	142.18	2.55	1272068	22799	.031	2.372
Wilbeck	199.98	142.18	7.69	1272068	68847	.031	2.372
Barber_ellipt.	130.26	142.18	2.55	1272068	22799	.061	2.372
Wilbeck_ellipt.	236.67	142.18	7.69	1272068	6884	.061	2.372

Table 4.2: Processing results, u_0 = 90 m/s, α = 60 deg

	total impulse [Ns]	P_H [Mpa]	P_s [Mpa]	F_H_av [N]	F_s_av [N]	t_b [ms]	t_D [ms]
SPH_unfiltered	119.68	210.49	3.45	961427	43106	0.105	3.062
SPH_filtered	118.25	81.03	3.41	229027	43115	0.153	2.953
Barber	79.72	123.13	2.17	1101643	19437	0.031	2.372
Wilbeck	173.79	123.13	6.66	1101643	59623	0.031	2.372
Barber_ellipt.	135.97	123.13	1.881	1272068	19437	0.072	2.372
Wilbeck_ellipt.	249.61	123.13	6.66	1272068	68847	0.072	2.372

Parameter Data Comparison
Table 4.3 to 4.6 offer a wider overview of the data. These tables contain all data collected over the different impact scenarios, but they only display one parameter. The two parameters chosen to be displayed are F_H in Table 4.3 and 4.4, as well as the total impulse in Table 4.5 and 4.6. It is important to note that the impact angles seen in the top rows are given as the angle between u_0 and a horizontal, similar to Figure 3.4 a).

Table 4.3: Peak forces, F_H, for all impacts at u_0 = 90 m/s

	a90	a80	a70	a60	a50	a40
SPH_unfiltered	1325176	915726	955645	961427	856755	903514
SPH_filtered	729992	339396	274527	229028	174548	178905
Barber	1272068	1252743	1195353	1101643	974461	817670
Wilbeck	1272068	1252743	1195353	1101643	974461	817670
Barber_ellipt.	1272068	1272068	1272068	1272068	1272068	1272068
Wilbeck_ellipt.	1272068	1272068	1272068	1272068	1272068	1272068

Table 4.4: Peak forces, F_H, for all impacts at u_0 = 180 m/s

	a90	a80	a70	a60	a50	a40
SPH_unfiltered	3599610	1864850	1935131	2051614	1649268	1851063
SPH_filtered	1622904	1188452	875825	792595	639907	556164
Barber	2819525	2776690	2649487	2441781	2159882	1812356
Wilbeck	2819525	2776690	2649487	2441781	2159882	1812356
Barber_ellipt.	2819525	2819525	2819525	2819525	2819525	2819525
Wilbeck_ellipt.	2819525	2819525	2819525	2819525	2819525	2819525

Figure 4.8 and 4.9 show a bar diagram that visualizes the change of the peak impact period for all impact angles and different models.

Table 4.5: Total impulse, j_{tot}, for all impacts at u_0 = 90 m/s

	a90	a80	a70	a60	a50	a40
SPH_unfiltered	148.56	143.76	133.15	119.68	101.78	81.51
SPH_filtered	148.52	142.36	131.91	118.25	100.50	80.28
Barber	92.17	91.09	87.49	79.72	72.48	61.63
Wilbeck	199.98	197.02	188.21	173.79	154.14	129.80
Barber_ellipt.	130.26	131.03	133.23	135.97	145.53	161.44
Wilbeck_ellipt.	236.67	237.96	242.03	249.61	262.30	283.50

Table 4.6: Total impulse, j_{tot}, for all impacts at u_0 = 180 m/s

	a90	a80	a70	a60	a50	a40
SPH_unfiltered	318.67	307.79	287.24	258.33	219.89	175.55
SPH_filtered	317	304.99	284.48	255.36	217.25	173
Barber	180.72	178.67	171.85	156.93	143.19	122.35
Wilbeck	394.25	388.47	371.29	343.16	304.8	257.19
Barber_ellipt.	253.28	254.88	259.5	265.57	285.73	319.83
Wilbeck_ellipt.	461.92	464.44	472.46	487.46	512.74	555.38

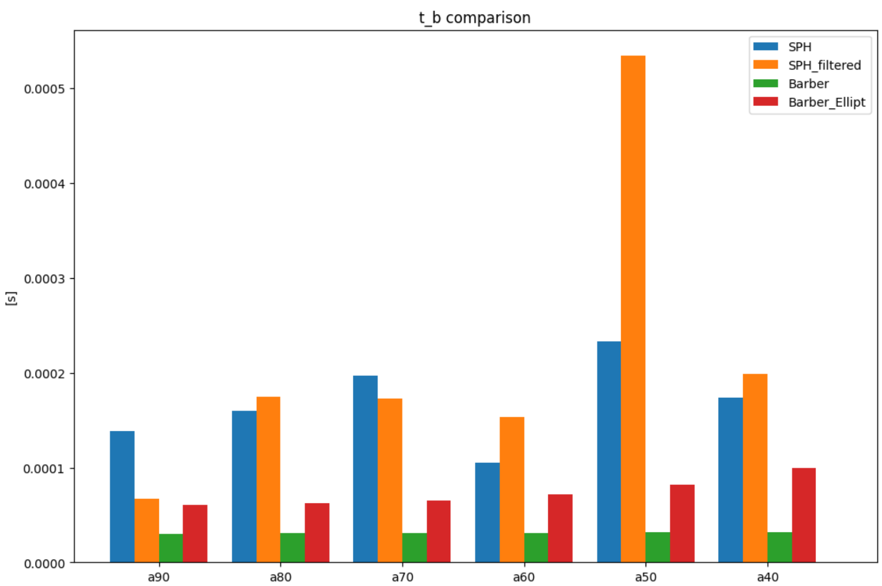

Figure 4.8: Peak pressure period t_b for 90 m/s impact velocity

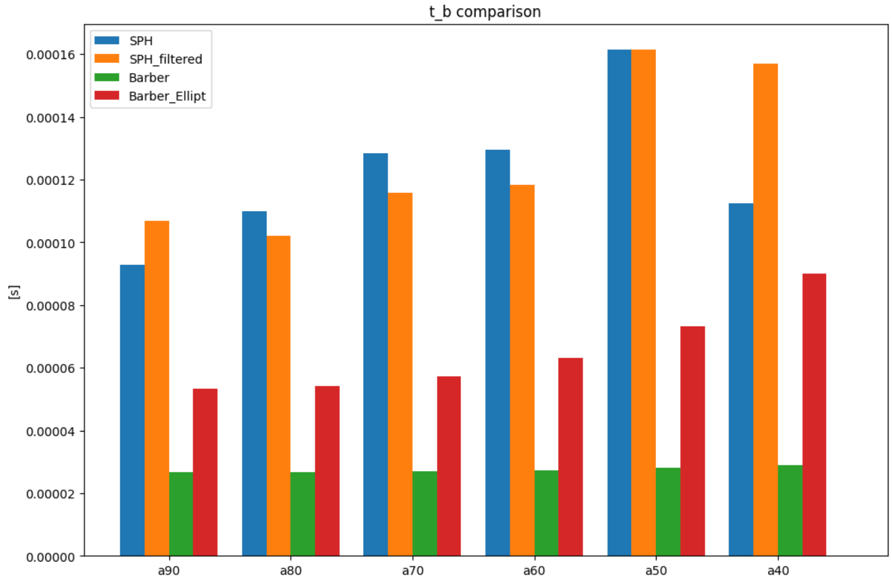

Figure 4.9: Peak pressure period t_b for 180 m/s impact velocity

4.2.2. Discussion

In this subsection, the data presented in subsection 4.2.1 is discussed. The discussion is divided in the same manner as the results, to offer a clear structure.

Scenario Data Comparison

Figure 4.2 and 4.3 depict the SPH data in blue and the filtered data in red. The values deduced from the data are portrayed as dashed lines.

The filtered data has smoothened the data successfully, the peak force however has been reduced drastically in both incidences. Table 4.1 and 4.2 contain the numerical values and present that the peak force of the raw data is 1.8 to 4 times higher than the force of the filtered data. Similar differences are present in all other impact scenarios. Therefore, the peak force of the filtered data set can be assumed to be incorrect. Increasing the cut-off frequency may lower the impact of the filtering process.

The averaged steady state force is almost identical. It is not possible to detect a difference visually, as the figure is too small. The numerical values Table 4.2 and 4.2, show that there is a sub 1% disparity between the filtered and unfiltered values.

There exists no objectively singular correct value for t_b or t_D as the force changes gradually. The peak force is reached almost instantaneously and only lasts a few tenths of a millisecond. It follows a dip until the steady state phase is reached. The peak pressure/force duration deduced from both the filtered and unfiltered data reliably creates values that lay in the low force period. No either of the values is consistently higher than the other. The impact duration was determined to be over once the force reached a tenth of the estimated steady state force. Durations determined by either data set lead to similar values, however not one of the both values is consistently higher than the other.

According to these findings, the data processing algorithms can consistently interpret both the filtered and unfiltered data. Peak forces are severely reduced by the filtering process, although it also successfully smoothens the data. All other parameters, on the other hand, are not consistently adulterated by the filtering process. Hence, the filtering process is not needed to interpret the data, but it does however increase the readability of the figures.

Figure 4.4 and 4.5 depict the SPH data in blue and the unfiltered data in orange. The green and red lines both represent the force history derived from Barber's and Wilbeck's models.

Both analytical models resort to the same timing functions and determine the peak force identically. Consequently, the peak force and time steps seen in the figures are coinciding. They only differ in the steady state force. Wilbeck's F_s values are consistently higher than Barber's. The figures also feature the total impulse. It seems that Wilbeck's model always overestimates the total impulse, whereas Barber's model underestimates it. Table 4.5 and 4.6 contain all total impulse values of all different impact scenarios tested. The table showcases that indeed, Wilbeck's values give an upper boundary of the total impulse, and Barber's model a lower boundary.

The peak force appears to be in good accordance with the unfiltered SPH data.

The timing of the SPH data and the analytical models can be compared by inspecting Figure 4.2 to 4.5 or by considering Table 4.5 and 4.6. When inspecting the peak pressure period as well as the impact duration, it becomes evident that the analytical models underestimate the timing for all impact scenarios.

Wilbeck's model creating an upper boundary for the total momentum and steady state force can be explained by its derivation. The Model assumes that all the momentum normal to the surface is transferred into the impulse. In reality, part of the bird mass is accelerated outwards due to the pressure wave, redirecting the momentum partially parallel to the surface. Some studies even opt to measure the remaining velocity to evaluate the momentum transfer into the structure. Additionally, the total momentum is divided by the squash time to determine F_s. The analytical model, nevertheless, underestimates the impact duration, leading to a further increase in the steady state force [37].

Barber's model creates a lower bound. This can be partially explained by the origin of the model. Barber models the bird as a continuous, incompressible, and irrotational stream of water and determines the pressure based on the velocity distribution over the plate. The method only records velocities within the projected boundary of the impactor. Therefore, the flow outside the boundaries is neglected, reducing the total recorded force.

The match of the impact force to the SPH data will be closely examined in the parameter-wise data comparison, as it allows the comparison of the data over the entirety of the impact scenarios.

The underestimation of the impact period is partially due to the arbitrary definition. If t_D was changed to be reached at 20% of F_s, a better match would have been achieved. Similarly, a better match of peak impact duration could be achieved by redefining the criteria used to determine t_b from the SPH data. It would also be possible to replace the impact duration of the analytical model with the steady state start marked by t_c, as this value is always higher than t_b. Ultimately, the changes would have been inconsequential for the methodology, as neither impulse nor peak forces are impacted by the change of timing parameters.

According to these findings, it can be concluded that timing and peak pressure do not differ between Barber's and Wilbeck's models, as they use the same functions. Additionally, Willbeck's model always overpredicts steady state force and total impulse, making it the most conservative analytical modeling method. The predicted peak forces appear to be accurate, whilst peak pressure duration and impact period are underestimated. Timing is inconsequential to the prediction of bird strike intensity, in any case.

Figure 4.7 and 4.6 both are the equivalent to the Figure 4.4 and 4.2, but plotting pressure instead of force. The pressure data is extremely noisy, making it impractical to come to any conclusion about steady state pressure or timing. Exclusively the peak pressure remains as a distinguishable value.

The study of Post [56] accredits the noise to the impact area modeling of his SPH model. The pressure is determined by dividing the force by the area, effectively multiplying the noise of both.

Due to the high noise of the data, all comparisons between numerical and analytical models are done using force data.

Parameter Data Comparison

When analysing the peak force values in Table 4.3 and 4.4, several observations can be made.

It is expected that the peak force decreases with decreasing impact angles. However, the unfiltered

SPH data contains uninspected spikes, which are removed by the filtering process. Equation 3.9 multiplied by the impact area A gives the peak force according to Wilbeck. Hence, Wilbeck's peak force decreases proportionally to the sin of the impact angle. Nevertheless, the analytical models that take the elliptical impact area into account have a constant peak force. Equation 4.2 defines the elliptical area, A_ell, as a function of the impact angle, showcasing that the area is proportional to the $\frac{1}{sin}$ of the impact angle. The area then decreases at the same rate as the peak pressure, leading to a constant peak force.

The hierarchy of the impacts differs between the unfiltered and filtered SPH data, as the unfiltered data contains spikes. The analytical models follow the hierarchy of the filtered data, provided the elliptical impact area is neglected.

$$A_{ell} = \pi \frac{a^2}{sin(\alpha)} \tag{4.2}$$

Table 4.5 and 4.6 contain the total impulse per scenario, allowing for yet another parameter to quantify impact intensity.

Similarly to the peak force, the total impulse is expected to decrease for decreasing impact angles. As seen in appendix A.2 the impulse is theoretically a function of the bird's momentum normal to the target. All data follows this trend, except for the analytical model that takes the elliptical area into account, which rises. This anomaly is caused by two factors. Firstly, the constant peak force. Secondly, an increased peak pressure period.

Ignoring the elliptical model, all data follows the expected hierarchy. Spikes that are present in the force data are not present, making the total impulse the better tool to compare the birdstrike intensity of different SPH analyses. The analytical models, in any case, do not differ in intensity between total impulse and peak force.

Figure 4.8 and 4.8 showcase the change peak impact duration for different impact angles and models. Equation 3.3 defined t_b as a function of the impactor radius and the release wave speed. Taking into account the elliptical impact area, the longest radius increases leading to an increase in peak pressure duration. Therefore, it can be assumed that the peak pressure duration increases with the decreasing impact angle.

Both the filtered and unfiltered SPH t_b data showcase a tendency to increase with a decreasing impact angle. As the timing functions ignore any changes to the impact area, they remain constant. However, the modified, elliptical models take the tendencies into account, following the numerical data.

It can be concluded that taking impact area changes into account improves the timing estimation, but has negative impacts on the bird strike intensity prediction. Additionally, it is shown that total impulse is the parameter to establish an impact hierarchy. It is also shown that Wilbeck's analytical model offers a consistent and conservative estimation of bird strike loads on flat rigid targets when compared to numerical SPH models.

4.3. Study of Chen et al. on the Flying-V

This section sums up the findings of Chen et al.'s 2022 study on bird impact on the Flying-V. Additionally, the same geometry is analyzed using the methodology of section 3.4. The results of the analysis are first discussed. Afterwards, the results are compared to Chen et al.'s findings to elaborate on the strengths and weaknesses of the methodology.

Figure 4.10 and 4.11 depicts the impact locations chosen as part of Chen et al.'s study on the Flying-V fuselage crash worthiness [20]. In the study, a detailed FEM model including strain-sensitive material models is developed, and several tests are run. Part of the study was to impact a Flying-V possible leading edge in several locations, to identify the critical location. Firstly, the leading edge is impacted along the center line, directly on the frame. Secondly, the window area is impacted on 16 different locations. The impact velocity was computed based on the regulations of CS 25.631 shown in subsection

2.2.2. Leading to an impact velocity of 70 m/s. The impact angle is based on the Flying-V's fuselage angle of 63.5 degrees.

Impacting the middle point leads to the highest peak in elastic strain energy (ALLSE), impacting the centre to the highest plastic strain energy (ALLPD). Chen et al. also plot the contributions of different parts to the energy. For both strain and plastic energy, the skin of section 1 was the biggest contributor [20].

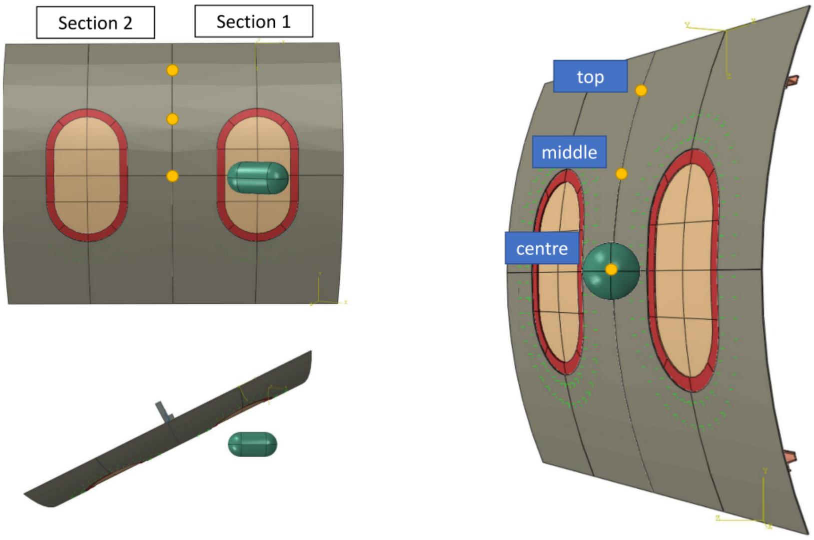

Figure 4.10: Impact location of Chen et al.'s center impact study [20]

Chen et al. divide the impacts into three groups. The horizontal group (1-4, 10-12), the vertical group (1, 5-9), and the diagonal group (13-16).

Comparing the horizontal impact locations, location 1 generated the highest plastic strain energy. Impacts on locations 2-4 generate less plastic strain energy than their counterparts of locations 10-12. Chen accredits this to the bird mass moving towards the stiffer window frame.

Location 6 of the vertical impact locations generates the highest plastic strain energy of all impacts. Thus, Chen et al. chose it as the critical impact location. However, the highest internal energy (ALLIE)) is reached by impacting location 1. The plastic strain energy rises from 1 to 6 and troops for the following impact locations, as they are approaching the stiffer window frame, leading to a reduced interaction between the polycarbonate window and the bird mass.

The peak plastic strain energy for the diagonal impacts is reached at point 15. Location 13's energy is notably lower, as the bird mass does not move over the window, but the frame and skin.

Chen et al. conclude that location 6 is the most critical impact location, with a plastic strain energy of 370J. Location 5 and 1 follow closely, with a plastic strain energy of 350 J and 340 J respectively [20].

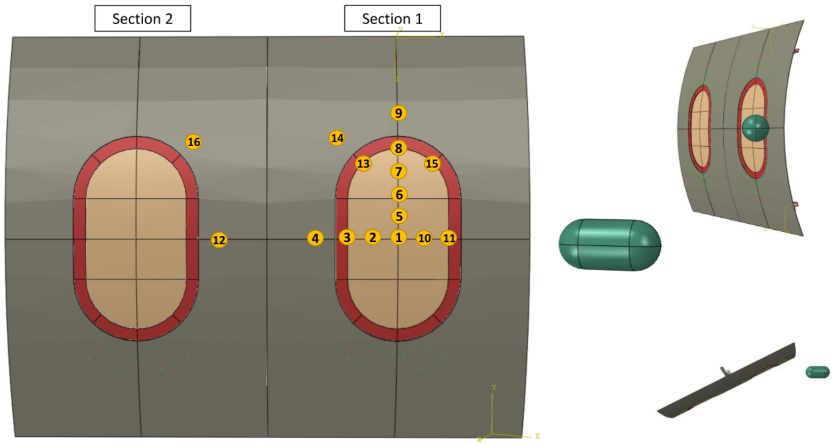

Figure 4.11: Impact location of Chen et al.'s window impact study [20]

4.3.1. Results & Discussion

Figure 4.12 depicts the results of the methodology described in section 3.4. The heatmap indicates the total impulse of the impact and the red arrow the flight path. To create the heatmap, Chen et al.'s model was transformed into an STL file the impact direction of his paper was copied. Figure 4.13 depicts the data captured by the heat map as a function of height.

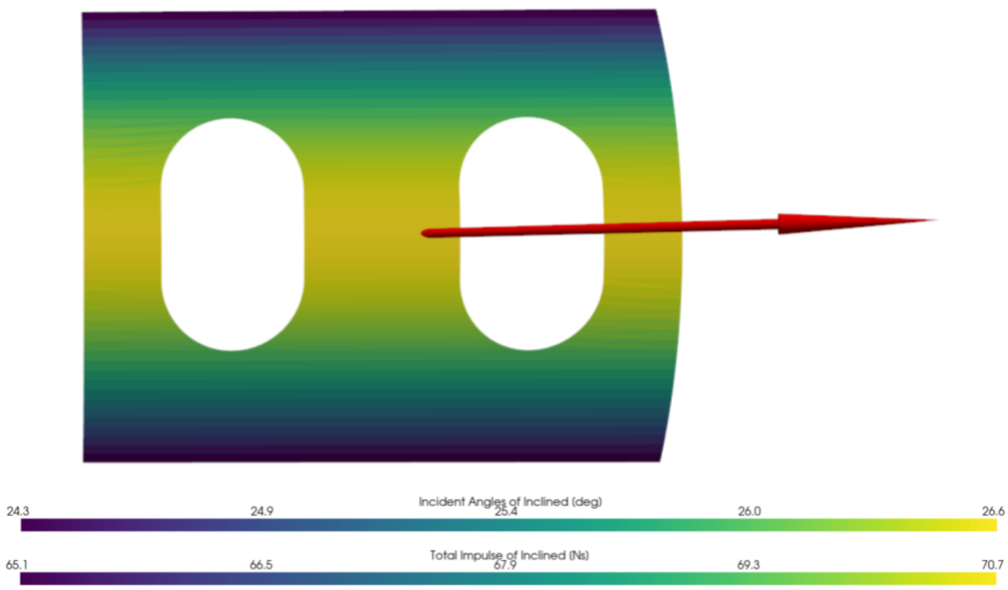

Figure 4.12: Bird strike heat map for impact impulse and incident angle, using Chen et al.'s structure and impact scenario [20]

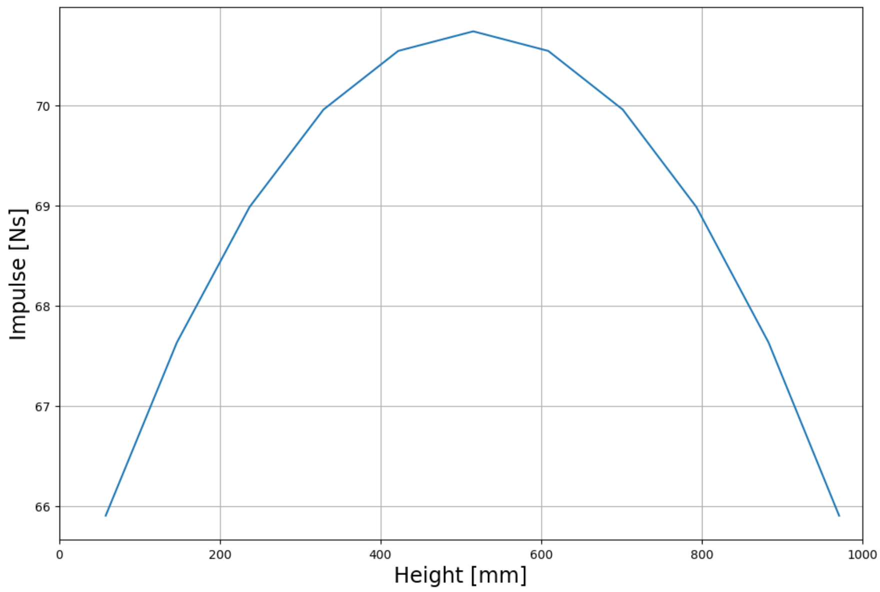

Figure 4.13: Impact impulse vs. Height of structure

When inspecting Figure 4.12, it is apparent that the incident angle and therefore the bird impact scenario remains constant along the horizontal axis of the leading edge. Additionally, there is very little curvature over the observed area, leading to a change of incident angle of about three degrees over the entire structure. This small change in angle also results in a very even distribution of the bird strike intensity. The peak of intensity is predicted to be along the center line of the structure.

Consequently, points 1-4 and 10-12 of Chen et al.'s study are all lying in the region where the most intense bird strike was predicted. When comparing the plastic strain energy recorded for all these points, the considerable effect of the structural response to the impact becomes apparent.

Figure 4.12 predicts equal bird strike intensity for all points, whereas the study finds the lowest plastic strain energy on this line to be 14 J for an impact on the center frame and the highest 340 J for point 1. If plastic strain energy is assumed as a parameter of the severity of the bird strike, the impact is almost 12 times worse despite the impact scenario being equal.

The critical location for impact is determined to be location 6, which lies outside the most severe region predicted by the methodology. Figure 4.13 shows the bird strike severity as a function of height. Knowing the window is 0.44 m high, it becomes apparent that the predicted bird strike intensity for all locations within the window only fluctuates by 1 Ns, only 1.4 % of the peak value of 7.5 Ns.

Even though location 1 is not the impact location that leads to the maximum plastic strain energy, it is the impact location that leads to the maximum peak in internal energy.

For the impact study along the frame, the center location leads to the peak plastic strain energy. Coinciding with the predicted peak bird strike intensity.
According to these findings, it can be concluded that the bird strike intensity parameter is not sufficient to determine a critical bird strike location. This limitation stems from the lack of knowledge of the hit structure. Despite this, the bird strike intensity correctly indicated the point with the peak in internal energy, as well as the peak plastic strain energy for impacts on equal structures. However, to conclude anything definitely, it is recommended that more impact studies are performed.

The methodology can provide additional insights into the impact scenarios. For example, the Flying-V will rarely fly perfectly horizontally. Any angle of attack will lead to a downward shift of the most intense region. With this knowledge, it is possible to predict that the most critical bird strike location will not be at point 6, but a point that lays below point 1.

In summary, even though the methodology can provide interesting contextual information for bird impact studies, the impact of structural interaction with the impact is too high to compare different regions solely using the bird strike intensity parameter, which assumes a rigid structure. Nevertheless, the data does not refute that the intensity parameter could be used to compare impacts for non-changing structures.

4.4. Methodology Demonstration

The following results and discussion use the methodology introduced in this study to compare bird strike intensity between the Flying-V and its TAW equivalent, the A380. To do so, a possible flight path for both aircraft as well as STL files of their geometries are used to create worst-case bird strike intensity maps. Table 4.7 and 4.8 show the velocity and angle of attack values used to create a possible flight path. The flight path data of the A380 is based on an altitude-velocity chart found in an online forum [3] and a manual published by Airbus [2]. The so reconstructed flight is a representation of a typical mission. To reconstruct a Flying-V flightpath, the A350 was copied. Based on the thesis of de Zoeten over the Flying-V flight performance [22] and consultations with C. Varriale and P. J. Proesmans from TU Delft, the angles of attack for Take-off and Approach were raised to 12.5 degrees. Both STL files are provided by a TU Delft internal collection. The Flying-V file is based on Laar et al.'s 2024 paper [42], and the A350 file is based on a file taken from grabcad [1].

Table 4.7: Flight path of A380 [3, 2]

	Take-off	Climbing 1	Climbing 2	Cruise	Approach 1	Approach 2
Velocity [m/s]	77	112	154	250	128	79
Angle of attack [deg]	10	20	20	3	20	10

Table 4.8: Flight path of Flying-V [3, 22]

	Take-off	Climbing 1	Climbing 2	Cruise	Approach 1	Approach 2
Velocity [m/s]	77	112	154	250	128	79
Angle of attack [deg]	12.5	20	20	3	20	12.5

The data collected during the methodology can also be utilized to gain additional insight. Old bird strike likelihood models, like the ones described by MC Govern [51], show that bird strike risk is proportional to the projected area, $A_{\text{proj.}}$, as well as the average velocity, $V_{\text{av.}}$, and time duration of the aircraft spent in the bird's airspace, T, as seen in Equation 4.4. These parameters effectively describe the volume of airspace the aircraft uses as it flies. Using these parameters, together with statistical data, allowed designers to predict the expected amount of bird strikes an aircraft would encounter in its lifetime. More modern studies like Metz et al.'s 2017 study [52] developed an algorithm to utilize radar data to determine real-time bird strike risk at the arrival and departure corridor of an airport. This study used more general data like wing span and aircraft height to create an estimated projected area.

PyVista has functions that can determine the area of each cell of an STL file. This data can be combined with the incident angle of each cell, determined by the methodology. Equation 4.3 shows how the projected area, $A_{\text{proj.}}$ of each cell and therefore of the total geometry is determined. Only the projected area of the hit cells must contribute to the total projected area.

$$A_{proj.} = \int_A \sin\alpha dA = \sum_{n=1}^{N_{hitel.}} A_n \cdot sin(\alpha_n) \qquad (4.3) \qquad P_{impact} \propto A_{proj.} \cdot V_{av.} \cdot T \qquad (4.4)$$

4.4.1. Results

Figure 4.14 and 4.15 depict a bird strike intensity map for each flight phase and an additional one, displaying all the worst-case impacts. Different perspectives of the intensity maps are displayed in appendix C.1. Section C.1 offers figures from different perspectives. Red areas mark where the impact intensity exceeds 90% of the maximal expected impulse. Areas that are not hit are opaque. The bar

[1] `https://grabcad.com/library?page=1&time=all_time&sort=recent&query=a350`,07.05.2024

diagram displayed in Figure 4.16 shows the hit area per flight phase. Figure 4.17 and 4.18 show how different flight phases contribute to the maximal impact heat map.

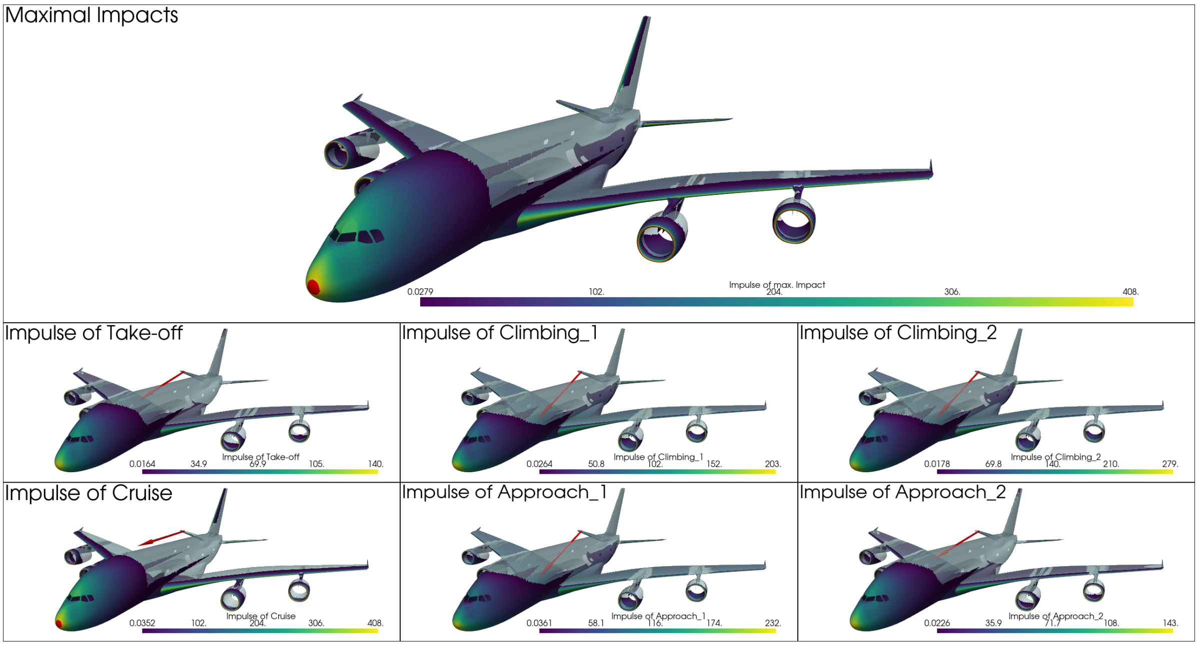

Figure 4.14: Bird strike intensity maps of A380 based on the flight path of Table 4.7

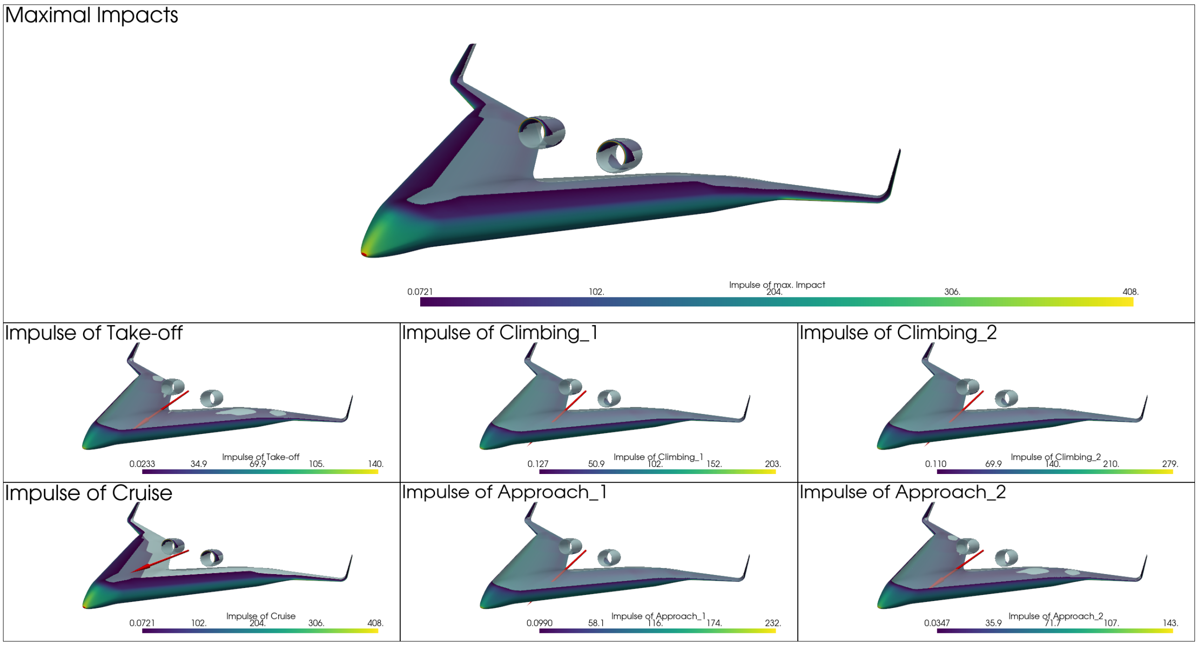

Figure 4.15: Bird strike intensity maps of Flying-V based on the flight path of Table 4.8

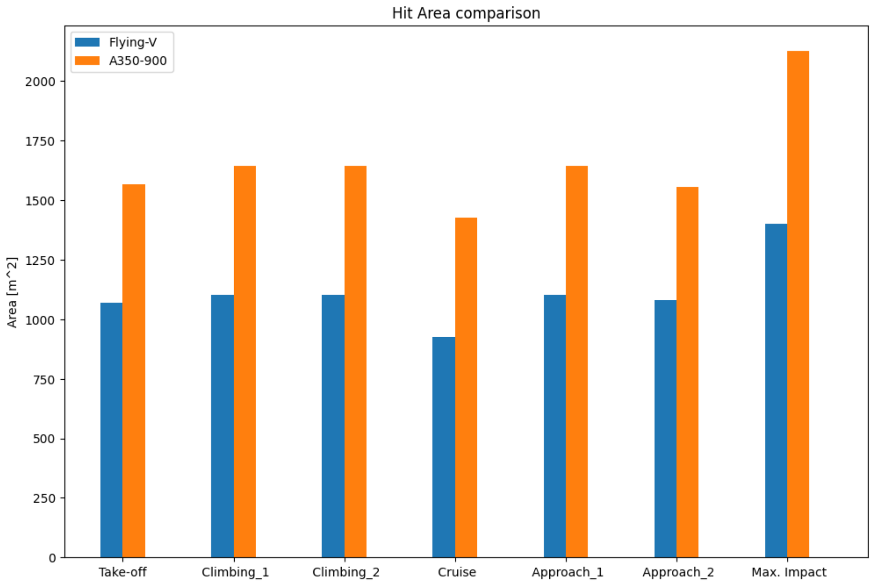

Figure 4.16: Hit area per flight phase for Flying-V and A380

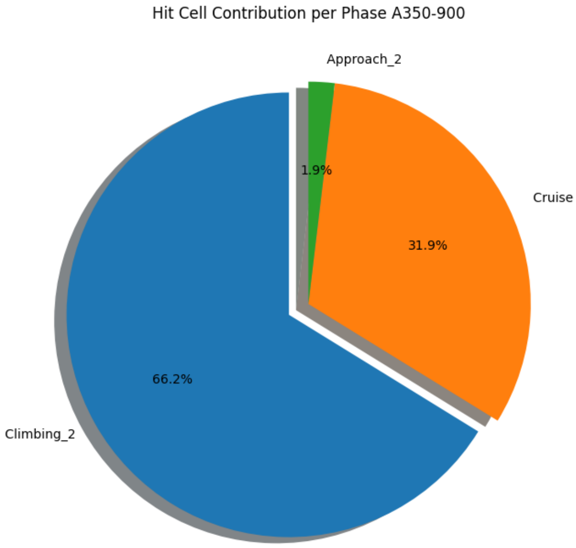

Figure 4.17: Area Percentage of max. intensity accounting to Worst case A380

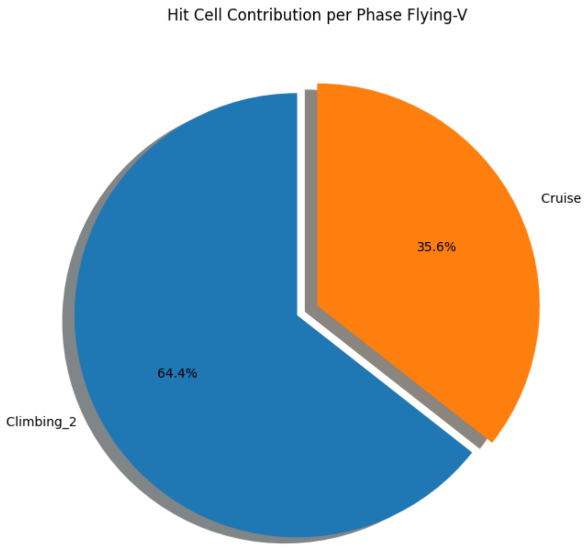

Figure 4.18: Area Percentage of max. intensity accounting to Worst case Flying-V

Table 4.9 contains the total surface and volume of both aircraft. Figure 4.19 and 4.20 depict the projected areas for all flight phases, with the aircraft split into different parts. The A380 is split into three parts: the wings, the fuselage and the empennage. As the Flying-V differs from the TAW configuration, another split was chosen. The Flying-V outer wing or empennage is separated from the fuselage or wing. Section C.2 contains figures showcasing how the aircraft were divided.

Table 4.9: STL mesh parameters

	A380	**Flying-V**
Total Surface Area [m^2]	4124.86	2241.66
Total Volume [m^3]	3735.89	1702.96

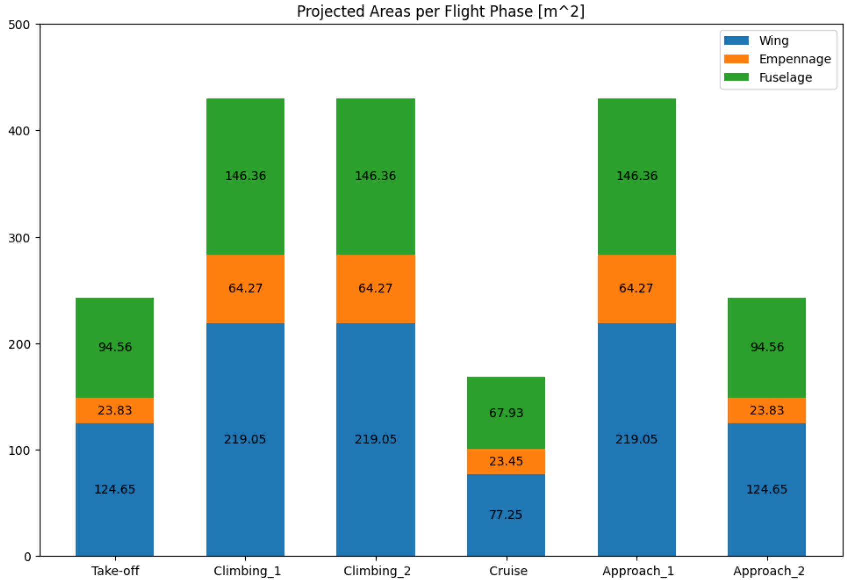

Figure 4.19: A380 projected areas for different flight phases and aircraft parts

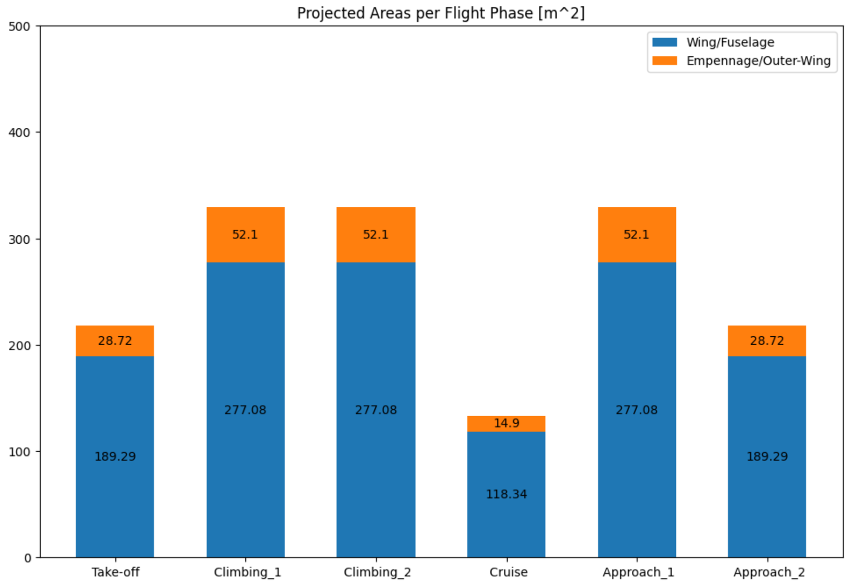

Figure 4.20: Flying-V projected areas for different flight phases and aircraft parts

The flight paths described in Table 4.7 and 4.8 contain conditions that are not relevant to the regulations. As described in subsection 2.2, only velocities under 8,000 ft are taken into account. The maximal allowed velocity under 10,000 ft is 128.1 m/s. Therefore, climbing_2 and cruise are irrelevant. According to Chen et al's study [20], the expected certification velocity of the Flying-V is 70 m/s. Using this velocity and the standard bird, a maximal impulse of 127 Ns for a normal impact can be expected. Only 7.1 m^2 or 0.8% of the Flying-V's impacted surface exceeds an intensity of 127 Ns. The same can be done for the A359-900, where 67.7 m^2 or 3.7% of all impacted surface area surpasses an impulse of 127 Ns.

4.4.2. Discussion

The figures depicted in subsection 4.4.1 are meant to demonstrate different ways to interpret the data amassed through the proposed methodology.

When inspecting figures 4.14 and 4.15, the effect of changing flight angles becomes apparent. For example, during most flight phases, the engines of the Flying-V are shielded by its body. Only shallow flight angles expose the top of the turbine housing. It can also be observed that higher angles of attack expose the underside of the aircraft. Figure 4.16 shows that all phases with the highest angle of attack expose the most area to bird strike.

Comparing the scalar bars of each part of Figure 4.14 and 4.15, it can also be seen that higher velocities lead to higher maximum impact intensities. The areas with the highest 10% expected impulse are marked red. All red-marked areas are exclusively seen in the cruise phase, further underlining the importance of velocity on bird strike intensity. It can also be observed that all red areas are at regions that are close to normal to the flight path.

Figure 4.16 shows that the exposed area of the A350 is much larger than the exposed area of the Flying-V. The contribution of different flight phases to the maximum impact, however, is very similar, as seen in figures 4.17 and 4.18. This can be accredited to the identical velocity profile since impact speed is the main contributor to impact intensity. The biggest contributor, area-wise, of worst-case impacts is climbing_2, with 66% for the A350 and 64% for the Flying-V. It follows the cruise phase, contributing 32% and 36%, respectively. Only for the A350, the approach_2 phase adds 2% of worst cases. Climbing_2 is the phase with the largest angle of attack and the highest velocity after the cruise phase, explaining its large contribution to the worst-case scenario.

The larger hit area of the A350 can be explained by the division between fuselage and wing. Whereas the Flying-V has an integrated fuselage, providing lift and space for passengers, the A350 divides these functions. This decision increases exposed area and volume, as shown in Table 4.9. This decrease in surface is an important factor in the increase in fuel efficiency of the Flying-V.

As shown in the beginning of this section, there exists a relation between the exposed area and the probability of bird impact. Papers that determine bird strike probability often use the projected area and the time and velocity spent at different altitudes as input to determine bird strike risk [10]. Hence, the data presented in Figure 4.19 and 4.20 can be used to make several remarks on bird strike likelihood. The phases cannot be compared to each other, since the velocity and duration in each phase vary. Each phase happens also at a different altitude. Therefore, different bird densities can be expected. In any case, it is possible to compare phases from the A380 and the Flying-V, as they have the same velocity.

The projected area of the A380 is higher during all flight phases when compared to the Flying-V. Consequently, it can be hypothesized that the Flying-V is less likely to hit a bird when compared to the A350.

The split into different aircraft parts hypothetically indicates the likelihood distribution of bird strike over the parts. The distribution shown in Figure 4.19 indicates that the wing will be hit most often, closely followed by the fuselage. Finally, the empennage only makes up a minute part of the projected areas. Table 2.2 shows more in dept hit distributions created by statistical data. As mentioned in subsection 2.1.2 the first three columns of Table 2.2 are created from data of airliners, operating aircraft similar to the A380. Comparing the results of Figure 4.19 to Table 2.2 some differences become apparent. Whilst the projected area of the wing is dominant, the most hit parts according to the airlines are the engines. This may be explained by the high volume flow of air through the engine, which sucks in birds. The data from Airbus suggests that the second most hit part is the fuselage. Boing and AOG however indicate the fuselage as the second most hit part. The fuselage is third, including windshields and radome. When adding the percentages of the engines to the wing, all three columns show an order of hit parts similar to Figure 4.19. Both Table 2.2 and Figure 4.19 agree that the empennage is the least likely part to be hit. A similarity between the prediction of Figure 4.19 is present, despite the large spread within the statistical data of Table 2.2.

Figure 4.20 shows the projected areas of the Flying-V. Here it becomes apparent that the wing, which includes the fuselage and cockpit, is the most likely part of the Flying-V to be hit. Whether the engines are sufficiently shielded or not, cannot be determined without taking the airflow into account.

Taking these considerations into account, it can be deduced that the Flying-V has not just disadvantages over the A380 considering bird strike. The exposed areas of the Flying-V include passenger windows. Whether or not it is possible to birdproof these areas without increasing the weight significantly remains unclear. Even though the forward-facing passenger cabinet is a big challenge, the total amount of area that is exposed to bird strike is significantly smaller than that of the A380. Due to the high sweep angle, the area that exceeds the maximal certification impulse of 127 NS of the Flying-V is only one-tenth times of the A380's. Critical areas, like the engines, are also more shielded than in the TAW configuration.

5 Conclusion

Developing new aircraft concepts requires new methods to satisfy the bird strike regulations. New shapes and flight paths result in altered bird strike scenarios. The manufacturer needs to be able to define the most critical bird strike scenarios to comply with regulations.

This thesis seeks to formulate a methodology capable of indicating bird strike intensity over the whole aircraft, solely based on geometry and flight path. To do so, analytical bird strike load models are analysed in terms of their ability to best express bird strike intensity. These models are used in conjunction with STL files, which describe the surface of an object. If a flight path is known, it is possible to map bird strike scenarios and intensity all over the geometry. By establishing a hierarchy using the intensity parameter, a worst-case heat map can be created.

The suitability of the decoupled analytical model of Wilbeck [66] and Barber [14] is analysed by comparing it to numerical data provided by the SPH models of Post's master thesis [56]. All models describe the impact of a bird on a rigid flat plate for different impact angles. Wilbeck's model assuming a circular cross-section is identified as the most suitable, as it consistently overestimates the pressures and impulses, making it the most conservative option. The best results have been achieved using the polynomial EOS system.

Bird strike intensity is best expressed as an impulse, as this value contains information about the impact scenario as well as the bird.

By comparing the intensity map to Chen et al.'s [20] detailed numerical study of critical bird strike locations on a possible Flying-V fuselage, the effectiveness of the intensity map was studied. It is apparent that the structural response to bird strike greatly varies depending on the impact location. The critical location determined by the analysis of 19 impact locations, actually lies slightly above the region with the highest predicted bird strike intensity.

However, the most critical impact aligns with the bird strike intensity map for impacts along the frame, as it offers very little structural variance.

The hierarchy of impact scenarios appears to be intact. However, large variations in impact angles may vary as different load paths are used, even though the impact happens at the same location.

The methodology was demonstrated with the Flying-V and the A350-900, allowing for a comparison of both designs. It was shown that the Flying-V design shields the engines from most bird impacts, unlike the A350. The maps could also show that higher velocity leads to intense impacts, whereas higher angles of attack lead to more exposed surface area. The A350 has a much higher exposed area when compared to the Flying-V, leading to the hypothesis that the Flying-V will be less likely to suffer from bird impacts.

Lastly, all flight conditions relevant for certification were analysed and it was shown that only 0.8% of impacted areas experienced bird strike as intense or higher as specified by the regulations. Therefore, a comprehensive definition of bird strike scenarios per area may allow manufacturers to locally lower the requirements dictated by the regulations.

In conclusion, the introduced methodology is not sufficient to pinpoint critical bird strike locations. The structural response differs significantly depending on the impact location. It does however provide flight state dependent bird strike scenario definitions, which may allow the manufacturers to locally assess the bird strike certification standards.

6 Recommendations

There are two types of recommendations on how the development should be continued. Firstly, recommendations on how to improve the existing methodology. Secondly, proposals for possible additions to the methodology that may lead to new output data.

To improve the significance of the data retrieved from this methodology the following is recommended:

- It may be possible to circumvent the methodology's limitation to large radii by discretising the bird similarly to Yu et al. [68].
- Further studies comparing the methodology data to FEM analyses should be conducted. This will be useful to understand the significance of the bird strike intensity map.

New additions to the methodology are proposed in the following list:

- It is advised to develop a methodology to take the structural response into account. The current method can only indicate theoretical bird strike intensity. With structural knowledge, it may be possible to predict bird strike severity.
- The current method solely defines not-exposed areas as areas that can not be hit by straight vectors if they are parallel to the flight direction. In reality, however, aircraft create high and low-pressure regions. Thus, it is recommended to analyse how these regions may alter the actual exposed areas.
- The methodology already provides a lot of data needed for bird strike likelihood study. With the inclusion of more detailed flight paths and some altitude-dependent bird strike data, it may be possible to create likelihood maps similar to the bird strike intensity maps. These maps could be combined with bird strike severity maps, making it possible to map bird strike risks over the whole aircraft.

References

[1] *2008 - 20015 Wildlife Strike Analysis (IBIS)*. Tech. rep. Montréal: International Civil Aviation Organization, May 2017. URL: `www.icao.int/IBIS`.

[2] *A350 AIRCRAFT CHARACTERISTICS AIRPORT AND MAINTENANCE PLANNING*. Blagnac, 2016. URL: `https://web.archive.org/web/20190531215550/https://www.airbus.com/content/dam/corporate-topics/publications/backgrounders/techdata/aircraft_characteristics/Airbus-Commercial-Aircraft-AC-A350-900-1000.pdf`.

[3] *A350 Takeoff VS*. 2020. URL: `https://community.infiniteflight.com/t/a350-takeoff-vs/420619`.

[4] *A350-900 - China Airlines 3D Model*. URL: `https://free3d.com/3d-model/a350-900-china-airlines-8358.html`.

[5] S. Abrate. “Soft impacts on aerospace structures”. In: *Progress in Aerospace Sciences* 81 (2016), pp. 1–17. ISSN: 03760421. DOI: `10.1016/j.paerosci.2015.11.005`.

[6] Airbus. *Flight Operation Briefing Notes*. Blagnac, Oct. 2004. URL: `https://www.skybrary.aero/sites/default/files/bookshelf/181.pdf`.

[7] *Airbus A350-900 - Lufthansa Group*. URL: `https://www.lufthansagroup.com/en/company/fleet/lufthansa-and-regional-partners/airbus-a350-900.html`.

[8] A Airoldi and B Cacchione. “Modelling of impact forces and pressures in Lagrangian bird strike analyses”. In: *International Journal of Impact Engineering* 32.10 (Oct. 2006), pp. 1651–1677. ISSN: 0734743X. DOI: `10.1016/j.ijimpeng.2005.04.011`.

[9] J R Allan. “THE COSTS OF BIRD STRIKES AND BIRD STRIKE PREVENTION”. In: *Human Conflicts with Wildlife- Symposium 2002* (Aug. 2000). URL: `https://digitalcommons.unl.edu/nwrchumanconflicts/18/`.

[10] Robert Andrews et al. “Three novel bird strike likelihood modelling techniques: The case of Brisbane Airport, Australia”. In: *PLoS ONE* 17.12 December (Dec. 2022). ISSN: 19326203. DOI: `10.1371/journal.pone.0277794`.

[11] Australian Transport Safety Bureau. *Australian aviation wildlife strike statistics 2008-2017*. Tech. rep. Canberra: Australian Transport Safety Bureau, 2019. URL: `www.atsb.gov.au`.

[12] Aviation Ornithology Group. *Aircraft Damages Caused by Birds*. 2006. URL: `https://otpugivanie.narod.ru/damage/eng.html`.

[13] R. B. Banks and D.V. Chandrasekhara. *Experimental investigation of the penetration of a high-velocity gas jet through a liquid surface*. Tech. rep. Evanston: Technological Institute, June 1962.

[14] J. P. Barber, H. R. Taylor, and J. S. Wilbeck. *BIRD IMPACT FORCES AND PRESSURES ON RIGID AND COMPLIANT TARGETS*. Tech. rep. Dayton: University of Dayton Research Institute, Nov. 1978.

[15] J. Benad. “The Flying V - A new Aircraft Configuration for Commercial Passenger Transport”. In: Deutscher Luft- und Raumfahrtkongress, 2015.

[16] Jonas Bertholdt. *Dataset for: Methodology to identify and quantify flight path depende bird strike scenarios over aircraft*. Version v1. May 2024. DOI: `10.5281/zenodo.11233626`. URL: `https://doi.org/10.5281/zenodo.11233626`.

[17] “Bird strike, a European risk with local specificities”. In: *European Aviation Safety Agency* (2013). URL: `www.aopa.de`.

[18] “Boeing AERO QTR_03 11”. In: *AERO Magazine* (2011), pp. 17–24. URL: `https://www.boeing.com/commercial/aeromagazine/articles/2011_q3/index.html`.

[19] CAAC. *Civil aviation regulation of China: 25–Airworthness standards of transport aircraft: CCAR-25-R4*. 2011.

[20] S. Y. Chen, W. Van De Waerdt, and S. G. P. Castro. “Design for bird strike crashworthiness using a building block approach applied to the Flying-V aircraft”. In: *Heliyon* 9.4 (2022), e14723. ISSN: 2405-8440. DOI: `https://doi.org/10.31224/2559`. URL: `https://www.sciencedirect.com/science/article/pii/S2405844023019308`.

[21] E C Cleary, S E Wright, and R A Dolbeer. *Wildlife Strikes to Civil Aircraft in the United STates 1990-1999*. Tech. rep. Washington, DC: Federal Aviation Administration National Wildlife Strike Database, 2000. URL: `https://nwrc.contentdm.oclc.org/digital/collection/NWRCPubs1/id/37245`.

[22] G J De Zoeten. *Comparative Flight Performance Evaluation of the Flying-V and a Reference Aircraft*. Tech. rep. URL: `http://repository.tudelft.nl/`.

[23] M Desiderio. *Flying-V Crashworthiness: a Preliminary Assessment*. Tech. rep. Delft: TU Delft, 2023.

[24] Deutsche Ausschuss zur Verhütung von Vogelschlägen im Luftverkehr (DAVVL). *Jahresbericht Statistik 2018*. 2018. URL: `https://www.davvl.de/sites/default/files/inline-files/2018_statistik.pdf`.

[25] Direction Générale de l’Aviation Civile. *Analyse du risque animalier en France 2010-2013*. Tech. rep. 2017.

[26] R A Dolbeer. *The History of Wildlife Strikes and Management at Airports*. Tech. rep. U.S. Department of Agriculture: Animal and Plant Health Inspection Service, 2013. URL: `https://digitalcommons.unl.edu/icwdm_usdanwrc/1459/`.

[27] R A Dolbeer et al. *Wildlife Strikes to Civil Aircraft in the United States, 1990–2019*. Tech. rep. Washington DC: Federal Aviation Administration National Wildlife Strike Database, 2021. URL: `https://rosap.ntl.bts.gov/view/dot/58293`.

[28] T. P. Dotman. *A Structural Sizing Methodology for the Wing-Fuselage of the Flying-V (MSc thesis)*. Delft: TU Delft Faculty of Aerospace Engineering, 2021.

[29] EASA. *Certification Specifications and Acceptable Means of Compliance for Large Aeroplanes (CS-25)*. 2021.

[30] EASA. *Certification Specifications for Normal Category Aeroplanes (CS-23) and Acceptable Means of Compliance and Guidance Material to the Certification Specifications for Normal-Category Aeroplanes (AMC & GM to CS-23)*. 2023.

[31] EASA. *Certification Specifications, Acceptable Means of Compliance and Guidance Material for Large Rotorcraft (CS-29)*. 2023.

[32] EASA. *Certification Specifications, Acceptable Means of Compliance and Guidance Material for Small Rotorcraft (CS-27)*. 2023.

[33] EASA. *Definitions and abbreviations used in Certification Specifications for products, parts and appliances CS-Definitions*. 2007.

[34] FAA. *Title 14 Aeronautics and Space Parts 1 to 59*. 2021. URL: `http://bookstore.gpo.gov%20https://www.ecfr.gov/on/2023-01-18/title-14`.

[35] T. Ferreira da Costa. *Crashworthiness Assessment of the Flying-V Tiago Ferreira da Costa*. Tech. rep. Delft: Delft University of Technology, 2024.

[36] M. Guida et al. *Certification by birdstrike analysis on C27J fullscale ribless composite leading edge*. 2013. DOI: `10.1016/j.ijimpeng.2012.10.002`.

[37] R. Hedayati and M. Sadighi. *Bird strike: An experimental, theoretical and numerical investigation*. Elsevier, WP Woodhead Publishing, 2016. ISBN: 978-0-08-100093-9.

[38] S. Heimbs. “Computational methods for bird strike simulations: A review”. In: *Computers and Structures* 89.23-24 (2011), pp. 2093–2112. ISSN: 00457949. DOI: `10.1016/j.compstruc.2011.08.007`.

[39] *INVESTIGATION REPORT Accident to the ROBIN-DR400-140B registered F-GNNE*. Tech. rep. Bureau d'Enquêtes et d'Analyses pour la sécurité de l'aviation civile, Apr. 2021. URL: www.bea.aero.

[40] A Kellogg and O Dimon. *Foundations of potential theory*. New York: Fredrick Ungar Publ., 1929.

[41] R. Koenderink. *Design Methodology for Unconventional Engine Mounting Structures, Including Crashworthiness Assessment*. Tech. rep. Delft: Technical University Delft, 204. URL: http://repository.tudelft.nl/..

[42] Y. Laar et al. "Aerodynamic Design of a Flying V Aircraft in Transonic Conditions". In: American Institute of Aeronautics and Astronautics (AIAA), Jan. 2024. DOI: 10.2514/6.2024-2669.

[43] M-A. Lavoie et al. *Review of existing numerical methods and validation procedure available for bird strike modelling*. Tech. rep. 4. 2007, pp. 111–118.

[44] M. A. Lavoie et al. "Bird's substitute tests results and evaluation of available numerical methods". In: *International Journal of Impact Engineering* 36.10-11 (Oct. 2009), pp. 1276–1287. ISSN: 0734743X. DOI: 10.1016/j.ijimpeng.2009.03.009.

[45] S J Leach et al. "Some Aspects of Rock Cutting by High Speed Water Jets". In: *The Royal Society of Publishing* 260.1110 (1966). URL: https://www.jstor.org/stable/73558.

[46] Leach S. J. and Walker G.L. "A discussion on deformation of solids by the impact of liquids, and its relation to rain damage in aircraft and missiles, to blade erosion in steam turbines, and to cavitation erosion - Some aspects of rock cutting by high speed water jets". In: *Philosophical Transactions of the Royal Society of London. Series A, Mathematical and Physical Sciences* 260.1110 (1966), pp. 295–310. DOI: https://doi.org/10.1098/rsta.1966.0051. URL: https://royalsocietypublishing.org/.

[47] J Lui et al. "Design of aircraft structures against threat of bird strikes". In: *Chinese Journal of Aeronautics* 31.7 (July 2018), pp. 1535–1558. ISSN: 10009361. DOI: 10.1016/j.cja.2018.05.004.

[48] R. Martinez-Val. *Flying Wings. A New Paradigm for Civil Aviation?* Tech. rep. Madrid: Universidad Politecnica de Madrid, 2007. DOI: 10.14311/914. URL: http://ctn.cvut.cz/ap/.

[49] F Marulo and M Guida. "Design criteria for birdstrike damage on windshield". In: *Advances in Aircraft and Spacecraft Science* 1.2 (Apr. 2014), pp. 233–251. ISSN: 22875271. DOI: 10.12989/aas.2014.1.2.233.

[50] F Marulo and M Guida. *Windshield Design Complying with Birdstrike Requirements*. Tech. rep. 2012. URL: https://www.researchgate.net/publication/324830533.

[51] S.A. McGovern. *Bird strike Design Manual*. Tech. rep. Bristol: British Aerospace Aircraft Group, June 1984, pp. 22–360.

[52] Apa) ; Metz et al. *Simulating the Risk of Bird Strikes*. Tech. rep. 2017, pp. 28–30.

[53] Isabel C. Metz et al. *The bird strike challenge*. Mar. 2020. DOI: 10.3390/aerospace7030026.

[54] L.S. Nizampatnam. "MODELS AND METHODS FOR BIRD STRIKE LOAD PREDICTIONS". PhD thesis. Wichita State University, Dec. 2007.

[55] G Palaia et al. "A conceptual design methodology for e-VTOL aircraft for urban air mobility". In: *Appl. Sci.* 11.22 (Nov. 2021). ISSN: 20763417. DOI: 10.3390/app112210815.

[56] M Post. *Model validation for bird strike crashworthiness*. Tech. rep. Delft: TU Delft, Feb. 2024.

[57] *Proposed Rules Bird Strike Requirements for Transport Category Airplanes*. Tech. rep. FAA, 2015. URL: https://www.federalregister.gov/documents/2015/07/20/2015-17404/bird-strike-requirements-for-transport-category-airplanes.

[58] A F El-Sayed. *Bird strike in aviation : statistics, analysis and management*. First Edition. John Wiley & Sons Ltd, 2019. ISBN: 9781119529828.

[59] C Silva et al. *VTOL Urban Air Mobility Concept Vehicles for Technology Development*. Tech. rep. NASA Ames Reseach Center, 2018. DOI: 10.2514/6.2018-3847.

[60] Sunil K. Sinha, Kevin E. Turner, and Nitesh Jain. "Dynamic loading on turbofan blades due to birdstrike". In: *Journal of Engineering for Gas Turbines and Power* 133.12 (2011). ISSN: 07424795. DOI: 10.1115/1.4004126.

[61] J Thorpe. *FATALITIES AND DESTROYED CIVIL AIRCRAFT DUE TO BIRD STRIKES, 1912 – 2002*. Tech. rep. Smallfield: International Bird Strike Commitee, May 2003.

[62] UK Civil Aviation Authority. *Reported birdstrikes 2012-2016*. URL: https://www.caa.co.uk/media/ynyhgvh0/20170316-reported-birdstrikes-2012-2016.pdf.

[63] R. C. J. Voeten. *A design methodology for un-conventional engine mounting structures*. Tech. rep. Delft: Technical University Delft, 2022. URL: http://repository.tudelft.nl/..

[64] E. Wallet. *Flying-V Composite*. URL: https://www.tudelft.nl/en/ae/flying-v.

[65] B.S. West and R.A. Brockman. *EVALUATION OF BIRD LOAD MODELS FOR DYNAMIC ANALYSIS OF AIRCRAFT TRANSPARENCIES*. Tech. rep. 1980.

[66] J. S. Wilbeck. *Impact Behavior of Low Strength Projectile*. Tech. rep. Wright-Patterson Airforce Base: Air Force Materials Labratory, U.S. Air Force Wright Aeronautical Labs, 1978.

[67] James S Wilbeck and Senior L Engineer James Rand Staff Engineer Mem ASME. *The Development of a Substitute Bird Model*. Tech. rep. 1981. URL: http://asmedigitalcollection.asme.org/gasturbinespower/article-pdf/103/4/725/5805082/725_1.pdf.

[68] Z. Yu et al. "Analytical determination of the critical impact location for wing leading edge under birdstrike". In: *Latin American Journal of Solids and Structures* 16.1 (Jan. 2019). ISSN: 16797825. DOI: 10.1590/1679-78255352.

A

Derivations Willbeck

A.1. Timing derivations

This section elaborates on the derivations of Willbeck's and Barber's timing equations taken from the 1978 paper [67].

Figure A.1 depicts the initial shock wave, the shocked area and the release waves that form shortly after impact. The shock wave leading the shocked region propagates with the velocity u_s, the release wave with c_r. Wilbeck assumes the steady state phase to start once the release waves reach point C, fully dissipating the shocked region.

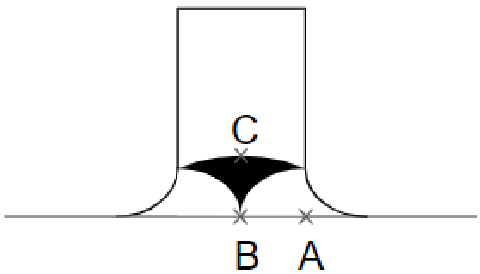

Figure A.1: Shock wave regime sketch taken from Figure 3.3 [66]

Equation A.1 expresses the distance from the target to point C, x_s. The relative velocity of the shock-wave to the target is the difference between the impact velocity, u_0, and the shock wave velocity u_s. To determine the distance between points A and C, x_r, the Pythagoras theorem is used as seen in Equation A.2.

$$x_s = (u_s - u_0) \cdot t_c \qquad \text{(A.1)} \qquad\qquad x_r = \sqrt{a^2 + x_s^2} \qquad \text{(A.2)}$$

The time needed for the release wave to reach the shock wave front can be calculated by dividing the wave speed, c_r, by the distance, x_r as seen in Equation A.3. By plugging int the terms for x_s and x_r determined by Equation A.1 and A.2 we arrive at Equation A.4.

$$t_c = \frac{c_r}{x_r} \qquad \text{(A.3)} \qquad\qquad t_c = \frac{a}{\sqrt{c_r^2 - (u_s - u_0)^2}} \qquad \text{(A.4)}$$

Equation A.5 defines the precise length of a projectile at which the shock wave reaches the end of the projectile at the same time as the release wave. In order to determine the critical aspect ratio the critical length is divided by the diameter leading to Equation A.6.

$$L_c = u_s \cdot t_c \qquad \text{(A.5)} \qquad\qquad (L/D)_c = \frac{a}{2\sqrt{c_r^2 - (u_s - u_0)^2}} \qquad \text{(A.6)}$$

A.2. Wilbeck load prediction derivations

The following models and derivations are taken from Wilbecks 1978 paper [66] on the impact behaviour of low-strength projectiles.

Hugonoit Pressure

Figure A.2 is used to derive the hugoniot pressure equation and depicts the shock wave as a 1-dimensional, adiabatic and irreversible flow. Parts (a) to (c) depict the same moment from different reference frames.

Figure A.2 (a) depicts the propagation of the shock wave from a reference system moving with the bird. The shock wave moves into region (1) with velocity u_s. As the reference system moves with the bird the mass in the non-shocked region appears to be at rest whereas the mass in region (2) moves with the particle velocity u_p. This showcases the change in velocity across the shock.

Figure A.2 (b) takes the perspective of the shocked region. The particle velocity in region (1) can be set equal to the initial velocity.

Figure A.2 (c) depicts the propagation of the shock wave from a reference system moving with the shockwave.

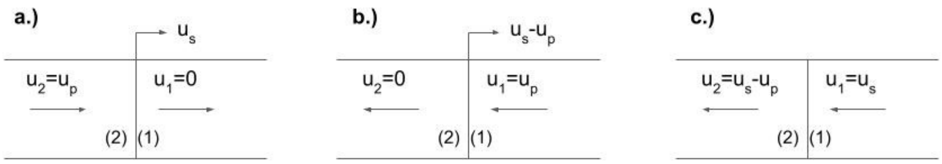

Figure A.2: Shock phase as one-dimensional flow

The perspective that is used to derive the pressures for the impact of cylinders on rigid plates is Figure A.2 (b). Using this reference frame the conservation of mass and momentum equations can be written as seen in equations A.7 and A.8.

$$\rho_1 u_s = \rho_2 (u_s - u_p) \quad \text{(A.7)} \qquad P_1 + \rho_1 u_s^2 = P_2 + \rho_2 (u_s - u_p)^2 \quad \text{(A.8)}$$

Combining equations A.7 and A.8 the pressure behind the shock can be defined as seen in Equation A.9.

$$P_2 - P_1 = P_H = \rho_1 u_s u_p \tag{A.9}$$

Steady state pressures

The change of momentum of the bird mass is equal to the impulse applied to the target, as described in Equation A.10. Solving the integral leads to Equation A.11. Assuming that the bird mass has no residual velocity, u, the applied impulse can be set equal to the bird mass multiplied by the impact velocity. Plugging in Equation 3.1, describing the impact duration, we arrive at Equation A.12. The average applied pressure, P_a can be defined by dividing the average applied pressure, F_a, by the impact surface area A.

$$\int_0^{t_D} F \, \mathrm{d}t = \int_{u_0}^{u} M \, \mathrm{d}u \quad \text{(A.10)} \qquad F_a t_D = M(u - u_0) \quad \text{(A.11)} \qquad F_a = \rho A u_0^2 \quad \text{(A.12)}$$

The derivation of the stagnation point pressure is based on the assumption that during the steady state phase, constant streamlines are formed throughout the flow. This assumption as well as the neglect of shear and body forces allows the use of Bernoulli's Equation A.13. The equation allows relating stream velocity and pressure along a streamline where K is constant. Equation A.14 is using Bernoulli's equation to compare two points along the same streamline, where P_0 and u_0 are at a point far away from the impact giving the atmospheric pressure and impact velocity. The pressure at the stagnation point is called stagnation pressure, P_s. AT this location the velocity is 0, leading to Equation A.15. Assuming that the material is incompressible allows to solve the integral leading to the stagnation point pressure Equation A.16. In reality, the density will increase with the increased pressure, therefore the stagnation point pressure of a compressible material will always be higher than the value determined with Equation A.16.

$$\int \frac{\mathrm{d}P}{\rho} + \int u \, \mathrm{d}u = K \quad \text{(A.13)} \qquad \int_{P_0}^{P} \frac{\mathrm{d}P}{\rho} + \int_{u_0}^{u} u \, \mathrm{d}u = 0 \quad \text{(A.14)} \qquad \int_{P_0}^{P_\mathrm{s}+P_0} \frac{d\mathrm{P}}{\rho} = \frac{u_0^2}{2} \quad \text{(A.15)}$$

$$P_s = \frac{1}{2} \rho u_0^2 \tag{A.16}$$

A.3. Wilbeck Model Adjustments

Table A.1 shows how different sources noted Leache's & Walker's pressure distribution formulation, as well as the version used in the birdpressure module.

Table A.1: Table listing all adjustments to Formulations used for Wilbeck's model

Equation	Wilbeck [66] (false)	Leach & Walker [45]	Used
Leach& Walker Equation 3.13	$\frac{1}{2}\rho u_0^2\left\{1-3\left(\frac{r}{\zeta_2 a}\right)^2+\left(\frac{\mathbf{r}}{\boldsymbol{\zeta}_\mathbf{2}\mathbf{a}}\right)^{\mathbf{3}}\right\}$	$\frac{1}{2}\rho u_0^2\left\{1-3\left(\frac{r}{\zeta_2 a}\right)^2+2\left(\frac{r}{\zeta_2 a}\right)^3\right\}$	$\frac{1}{2}\rho u_0^2\left\{1-3\left(\frac{r}{\zeta_2 a}\right)^2+2\left(\frac{r}{\zeta_2 a}\right)^3\right\}$

B

Derivations for barber model

B.1. Barber cp

When taking into account the assumption of potential flow made in Barber's analytical model [14], the Bernoulli equation can be used to derive a formulation of the pressure coefficient that solely depends on the flow velocity. The Bernoulli equation for potential flow can be expressed as seen in Equation B.1. Here P_tot is the total pressure, P is the static pressure and $1/2\rho V^2$ is the dynamic pressure. As seen in Equation B.2, the total pressures of two points can be assumed to be constant for potential flow. Therefore the difference in static pressure can be expressed as seen in Equation B.4.

$$P_{tot} = P + \frac{1}{2}\rho V^2 \quad \text{(B.1)} \qquad P_{tot1} = P_{tot2} \quad \text{(B.2)}$$

$$P + \frac{1}{2}\rho V^2 = P_\infty + \frac{1}{2}\rho V_\infty^2 \quad \text{(B.3)} \qquad P - P_\infty = \frac{1}{2}\rho(V_\infty^2 - V^2) \quad \text{(B.4)}$$

The pressure coefficient, C_p, is defined as seen by B.5 and can be rewritten to be a function of free stream velocity V_∞ and the velocity at an arbitrary point, V.

$$C_p = \frac{P - P_\infty}{\frac{1}{2}\rho\infty V\infty^2} = 1 - \frac{V^2}{V\infty^2} \quad \text{(B.5)}$$

B.2. Barber Changes

Table A.1 lists mistakes made by the copying of different formulations. In the first row, Kellogg's formulation to express the velocity field in w direction is shown. The formulation was falsely copied in Hedayati's book on bird strike [37]. In row two the pressure coefficient is shown. Both Hedayati [37] and Barber et al. [14] give an incorrect formulation. Barber, however, uses the correct version in the pseudo-code he published with his paper [14]. The derivation of the correct version can be found in the subsection above.

Table B.1: Table listing all adjustments to Formulations used for Barber's models

Equation	Hedayati [37] (false)	Barber [14]	Used
Kellogg Equation 3.22	$\frac{q''}{4\pi} \ln\left\{\frac{[r_3+(\eta_2-y)][r_1+(\eta_1-y)]}{[\mathbf{r_4}+(\eta_2-y)][\mathbf{r_2}+(\eta_1-y)]}\right\}$	$\frac{q''}{4\pi} \ln\left\{\frac{[r_3+(\eta_2-y)][r_1+(\eta_1-y)]}{[r_2+(\eta_2-y)][r_4+(\eta_1-y)]}\right\}$	$\frac{q''}{4\pi} \ln\left\{\frac{[r_3+(\eta_2-y)][r_1+(\eta_1-y)]}{[r_2+(\eta_2-y)][r_4+(\eta_1-y)]}\right\}$
Pressure Coefficient Equation 3.23	$\frac{V^2+W^2}{U_\infty^2}$	$\frac{V^2+W^2}{U_\infty^2}$	$1 - \frac{V^2+W^2}{U_\infty^2}$

C
Additional Figures

C.1. Intensity maps different perspectives

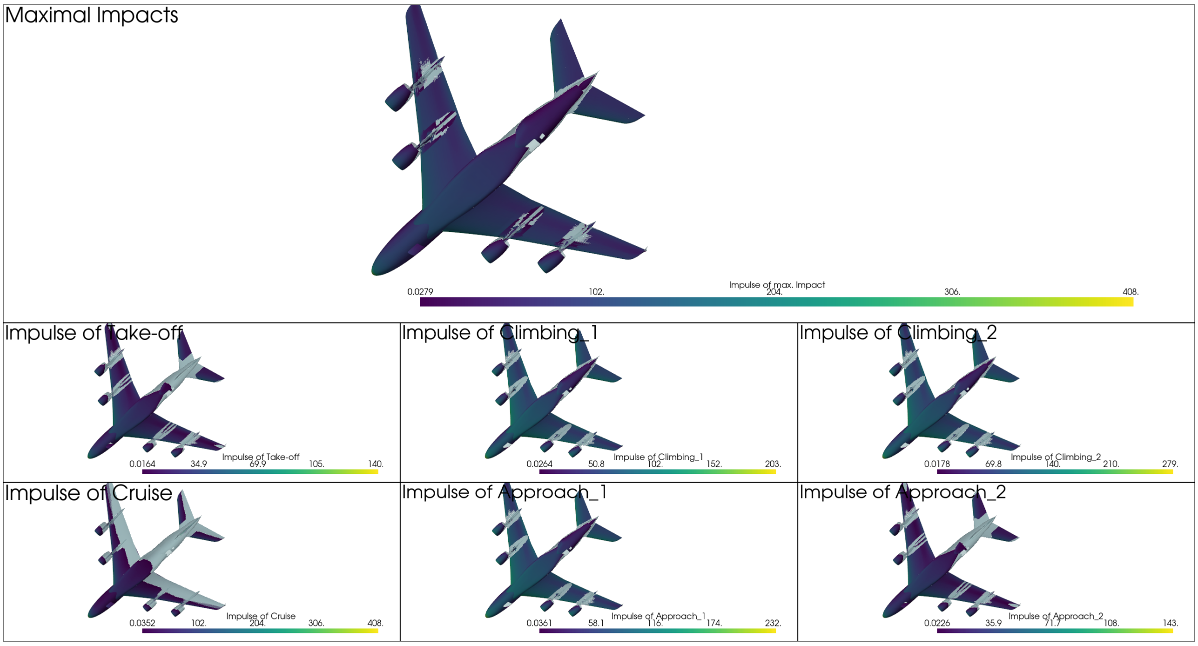

Figure C.1: Bird strike intensity maps of A950-900 based on the flight path of table 4.7, bottom view

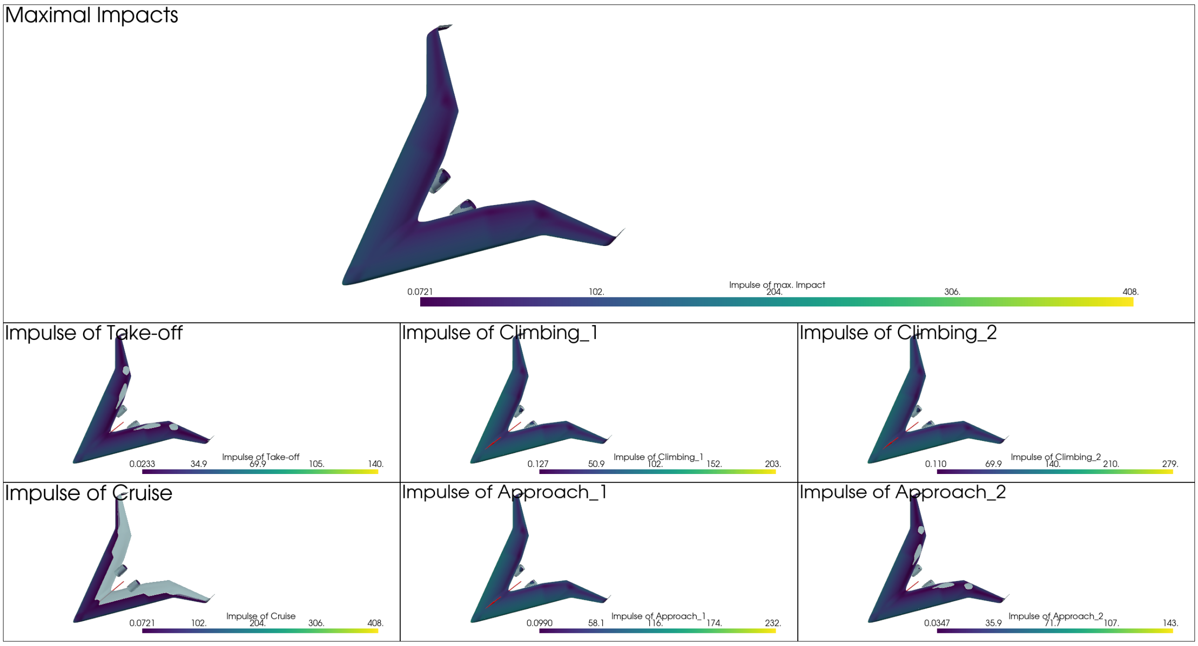

Figure C.2: Bird strike intensity maps of Flying-V based on the flight path of table 4.8, bottom view

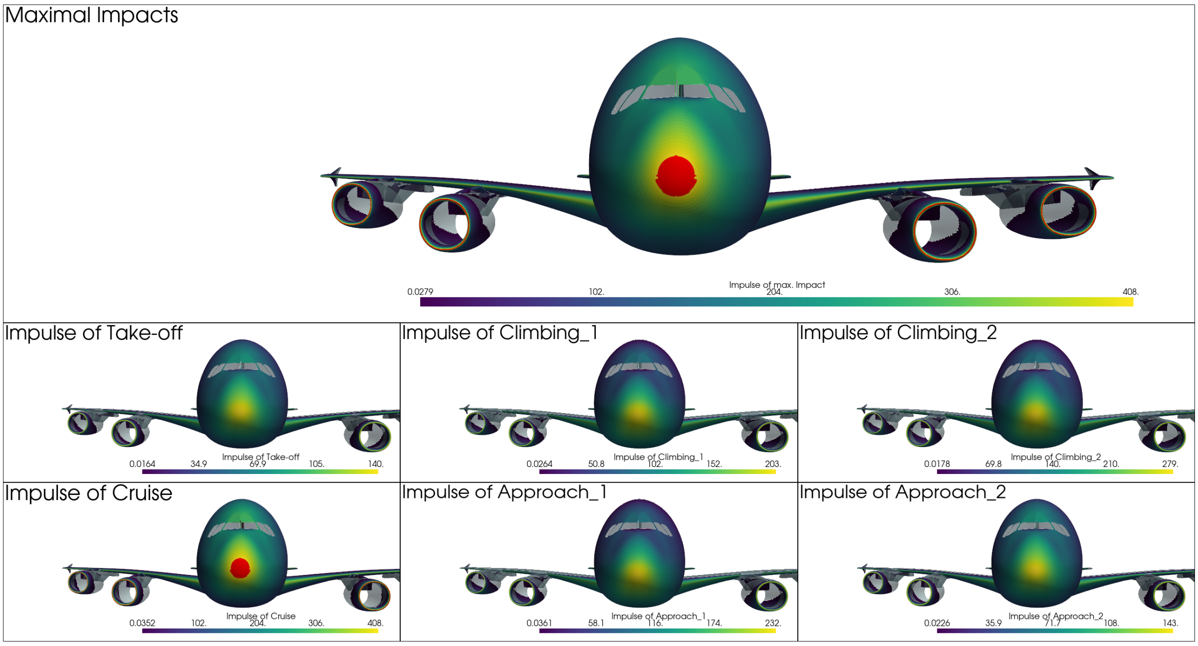

Figure C.3: Bird strike intensity maps of A950-900 based on the flight path of table 4.7, front view

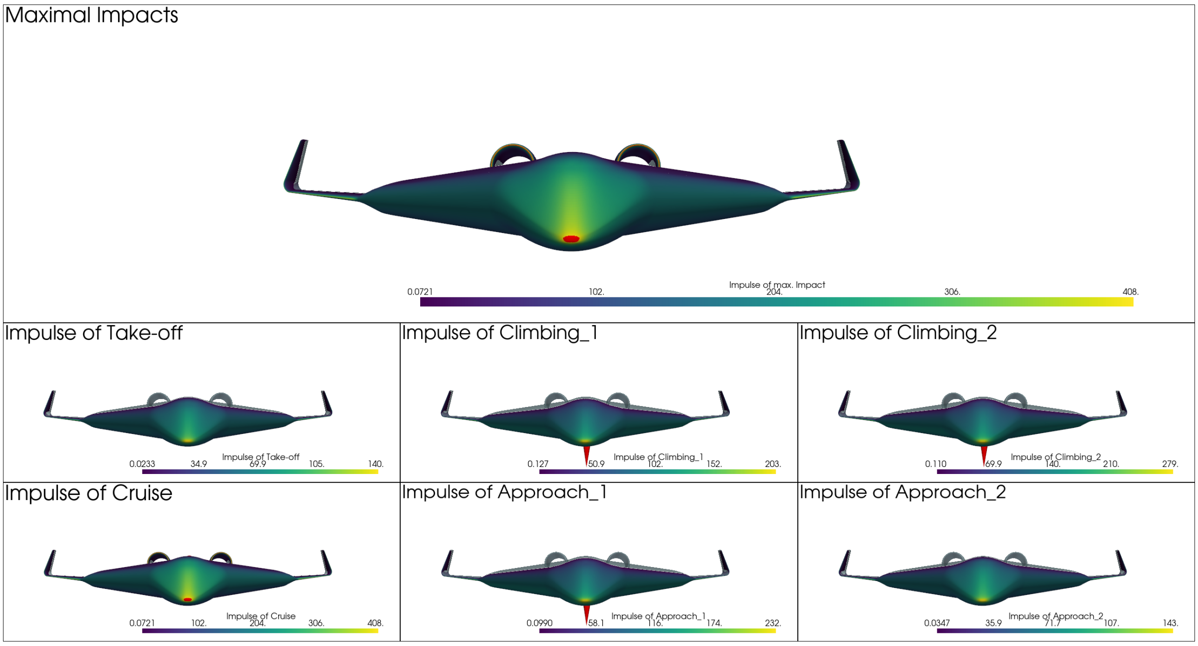

Figure C.4: Bird strike intensity maps of Flying-V based on the flight path of table 4.8, front view

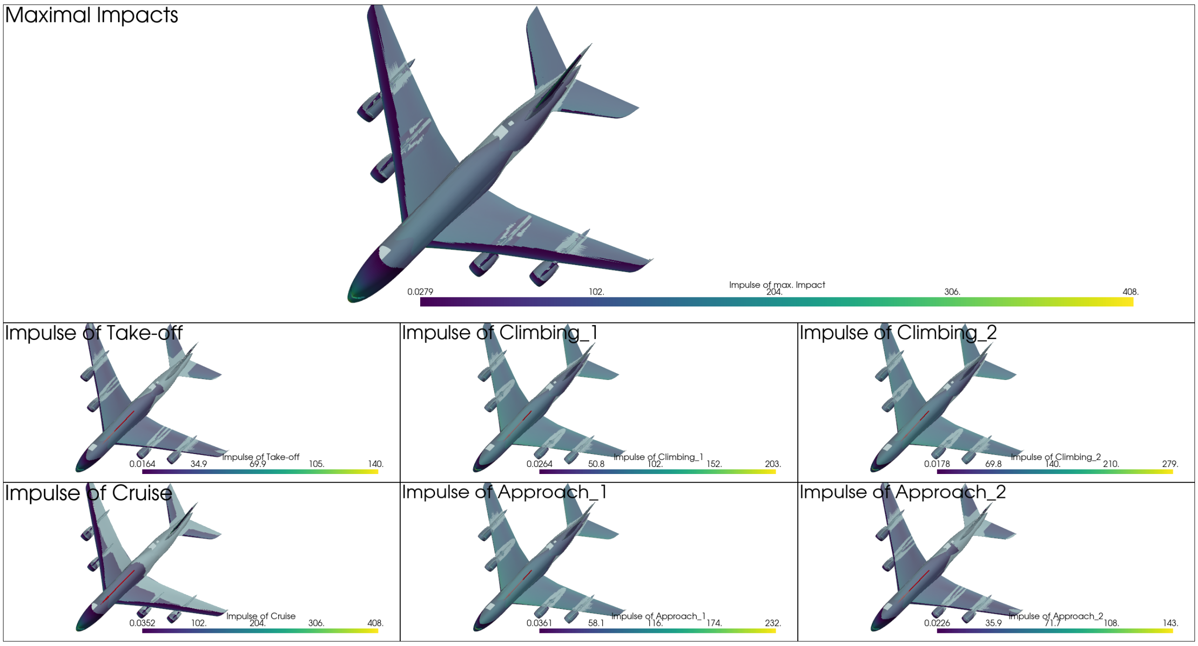

Figure C.5: Bird strike intensity maps of A950-900 based on the flight path of table 4.7, top view

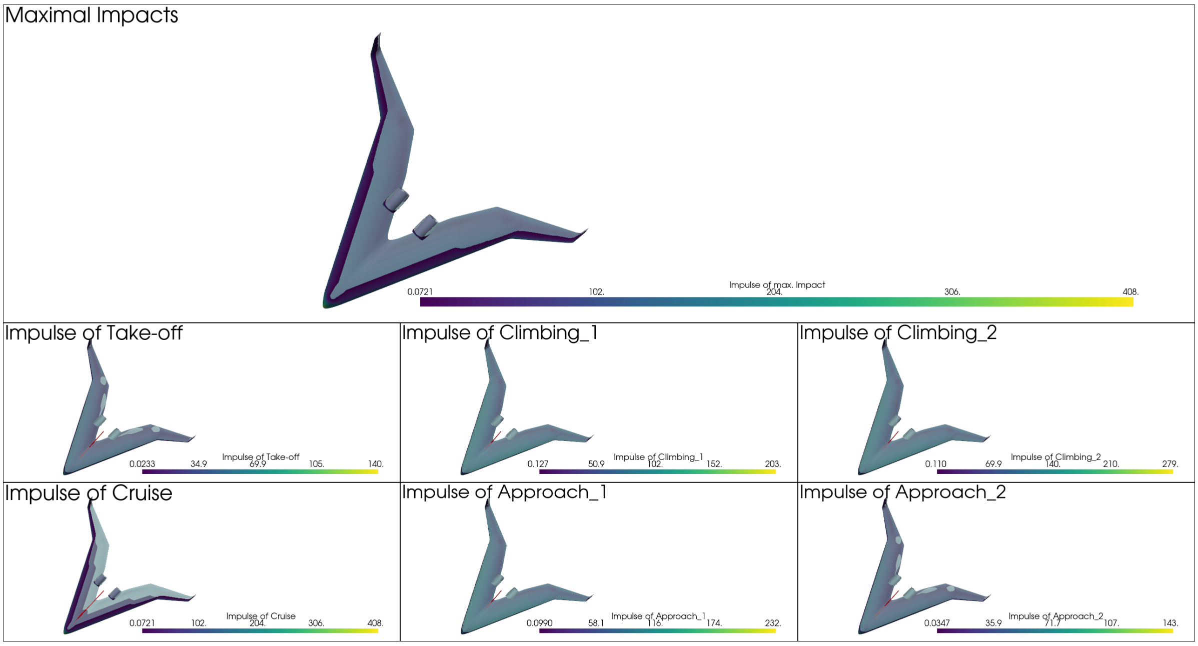

Figure C.6: Bird strike intensity maps of Flying-V based on the flight path of table 4.8, top view

C.2. Projected Area split

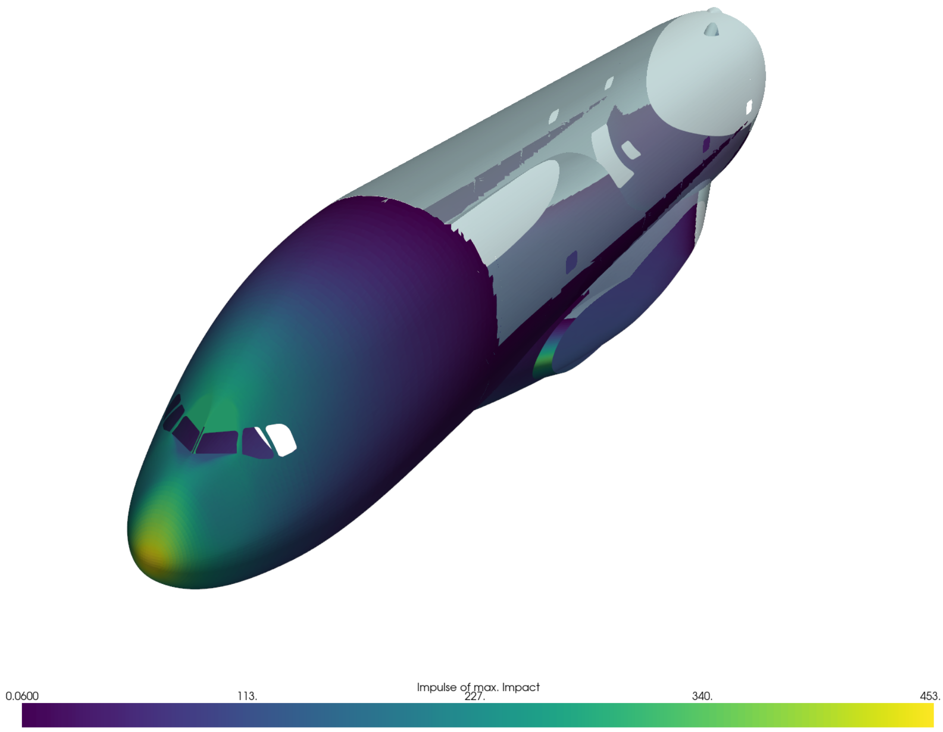

Figure C.7: A350-900 fuselage split used for projected area calculation

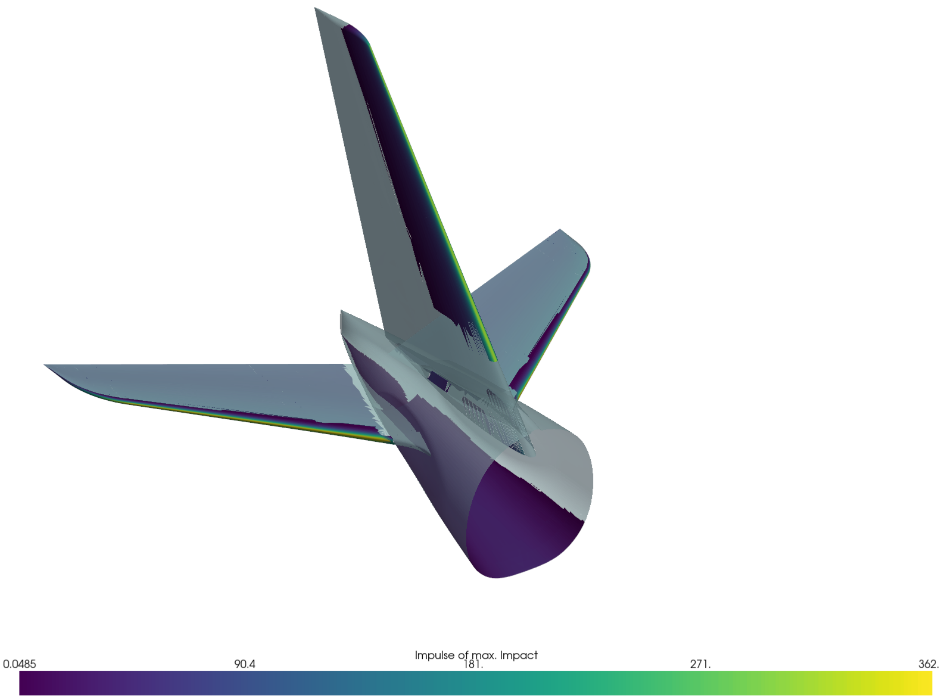

Figure C.8: A350-900 empennage split used for projected area calculation

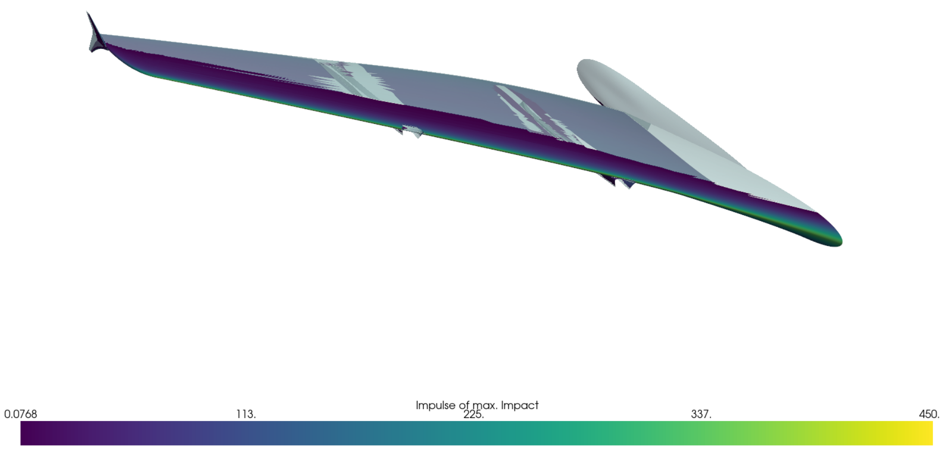

Figure C.9: A350-900 wing split used for projected area calculation

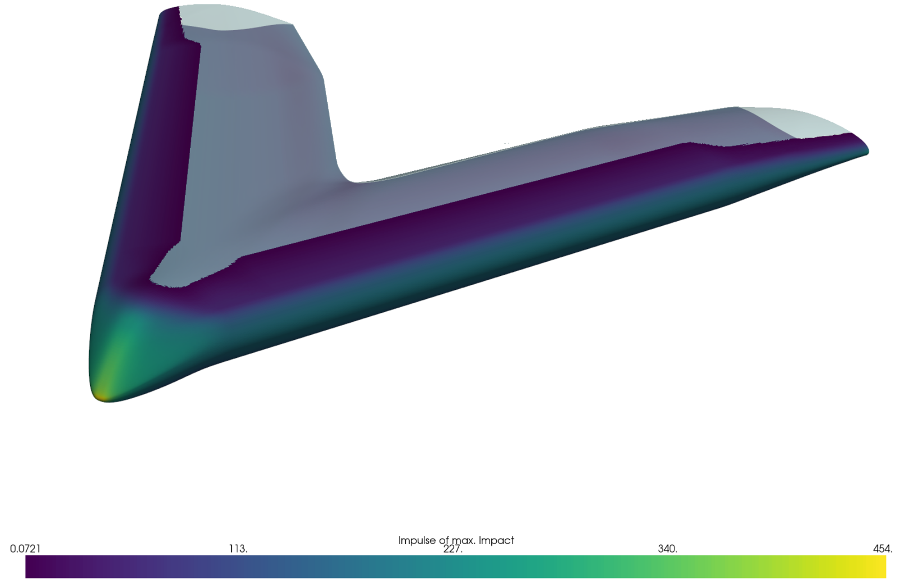

Figure C.10: Flying-V fuselage/wing split used for projected area calculation

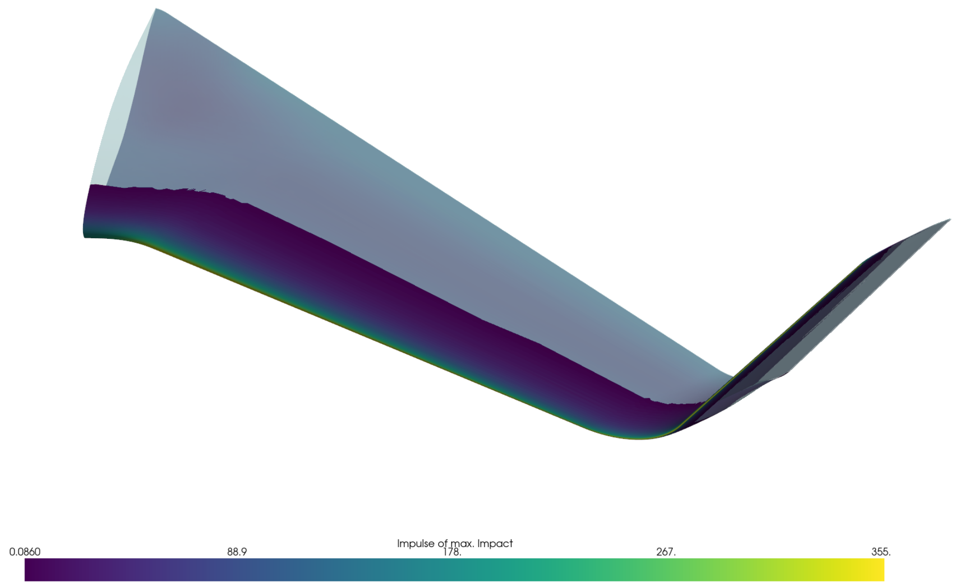

Figure C.11: Flying-V aft wing/empennage split used for projected area calculation